Earth and Planetary Science Letters
November 2023, Volume 621 Pages 118380 (11p.)
https://doi.org/10.1016/j.epsl.2023.118380
https://archimer.ifremer.fr/doc/00855/96678/

Evidence for low Vp/Vs ratios along the eastern Romanche ridge-transform intersection in the equatorial Atlantic Ocean

Yu Zhiteng [1, 2, *], Singh Satish C. [3], Maia Marcia [2]

[1] Key Laboratory of Submarine Geosciences, Second Institute of Oceanography, Ministry of Natural Resources, 310012 Hangzhou, China
[2] Geo-Ocean UMR6538, CNRS-Ifremer-UBO-UBS, 29280 Plouzané, France
[3] Université Paris Cité, Institut de Physique du Globe de Paris, CNRS, 75238 Paris, France

* Corresponding author : Zhiteng Yu, email address : ztyu@sio.org.cn

Abstract :

Very long oceanic transform faults do not just offset mid-oceanic ridges by hundreds of kilometers, but they also induce variations in the lithospheric structure and affect mantle melting, and hence the crustal accretion at the ridge-transform intersection (RTI). However, the deep structure of large offset RTIs remains unknown. Here, we present three-dimensional seismic tomography results (P- and S-wave velocities, Vp, Vs) in the vicinity of the eastern Romanche transform and the Mid-Atlantic Ridge in the equatorial Atlantic Ocean, using arrival times from microearthquakes recorded by a recent temporary array of seafloor seismometers. We find that normal to low Vp/Vs ratios (~1.7) are observed at the Mid-Atlantic Ridge, representing weak serpentinization and the dominant magmatic processes, whereas high Vp/Vs ratios (~1.8-1.95) are observed west of the RTI, at the eastern termination of the 2016 7.1 earthquake. However, unusually low Vp/Vs ratios (~1.6-1.7) are observed at 0-15 km depth and in the region of the 2016 7.1 earthquake rupture zone. We suggest that the unusually low Vp/Vs ratios result from the presence of thick cracks at shallow depths (0-8 km) and/or the enrichment of orthopyroxene in the deep mantle (8-15 km).

Highlights

► 3-D Vp and Vs models for the Romanche eastern ridge-transform intersection. ► Low Vp/Vs ratios (~1.6-1.7) at depths of <15 km along the transform are observed. ► The low ratios may be due to thick cracks and/or orthopyroxene enrichment.

Keywords : oceanic transform faults, fracture zones, mid-ocean ridge processes, seismic tomography, ridge-transform intersection, earthquakes

1 Introduction

Oceanic transform faults represent one of the three first-order plate boundaries on Earth and are often bounded by two mid-ocean ridge segments (Wilson, 1965). In comparison to the previous simple and "conservative" mode of transform faults (Wilson, 1965), the latest studies on transform faults have illustrated a much more complicated formation and evolution process (Gregory et al., 2021; Grevemeyer et al., 2021; Hicks et al., 2020). Many seismic tomography studies have revealed a reduced velocity zone beneath the active transform valley at slow-slipping transform faults, which is mainly attributed to a thinned crust underlain by a strongly serpentinized mantle (Detrick et al., 1993). A recent seismic refraction study on the Romanche transform fault also reveals a low P-wave velocity zone at 0~9 km depth beneath the transform valley (Gregory et al., 2021), but it is interpreted to be due to the presence of fractured mafic materials (Gregory et al., 2021), similar to that at fast-slipping Gofar transform fault (Roland et al., 2012). In addition, Wang et al. (2022) further observed that this low P-wave velocity zone can extend down to ~60 km depth, which could be due to mantle hydration and water-induced melting. Furthermore, some recent seismic refraction studies indicate relatively normal crustal thicknesses across fracture zones (inactive transform traces) (Growe et al., 2021; Marjanović et al., 2020). Grevemeyer et al. (2021) suggested that crustal thickening occurs at the ridge-transform intersection (RTI). However, the seismic structures of the crust and upper mantle beneath the RTI are unconstrained due to limited seismic experiments.

Previous works have indicated that the P- to S-wave velocity (Vp/Vs) ratios can be used to discriminate the lithological composition in the crust and mantle (Christensen, 2004; Grevemeyer et al., 2018; Hacker and Abers, 2004). The Vp/Vs ratio for the normal gabbroic crust is <1.9 (Becker et al., 1989; Grevemeyer et al., 2018; Johnston and Christensen, 1997). However, the Vp/Vs ratio for the mantle serpentinized peridotite is typically ≥1.9, reaching as high as 2.2 (Christensen, 2004). In contrast, the large aspect ratio of cracks (Takei, 2002) and the presence of gas (Ito et al., 1979; Wang and Nur, 1989) can remarkably reduce the Vp/Vs ratios.

In this study, we performed seismic tomography to obtain detailed three-dimensional (3-D) P-wave (Vp) and S-wave velocity (Vs) models and Vp/Vs ratios in the shallow lithosphere, to investigate the seismic properties of the eastern RTI of the Romanche transform fault and the nearby ridge segments. Together with the high-resolution bathymetry data and geological data from submersible dives and rock sampling, we provide evidence for the tectonic and magmatic processes of the eastern Romanche RTI, shedding new light on the understanding of the ridge and transform systems.

2. Study area

The Romanche transform fault, located in the Equatorial Atlantic Ocean, is one of the largest oceanic transform faults on Earth (Fig. 1a). It offsets the slow-spreading Mid-Atlantic Ridge (MAR) by ~880 km (Fig. 1a), with a maximum age contrast of ~45 Ma, assuming the slip rate of ~3.2 cm/yr (DeMets et al., 2010). Our study region lies in the vicinity of the eastern Romanche RTI, where the transform valley width can reach up to ~20 km (Fig. 1b). A large-scale oceanic core complex is present on the outside corner (Fig. 1b). Two oblique hills west of the RTI may represent the fragments of ancient oceanic core complexes (Fig. 1b). To the north of the transform valley, two transverse ridges and a suspended valley are found (Fig. 1b), representing the trace of the migration and reorientation of the transform 8-10 Ma ago (Bonatti et al., 1994). To the south, the absence of basaltic crust indicates that the mantle may have undergone a low degree of melting (Bonatti et al., 2001), consistent with the results from the numerical modelling of the RTI (Ligi et al., 2008, 2005). A large volume of peridotites was dredged at its 30-km-wide southern flank from transform fault to fracture zone (Bonatti et al., 2001, 1996; Maia and Brunelli, 2020; Yu et al., 2021) (Fig. 1b). New rock samples collected by the Nautile dives during the SMARTIES cruise (Maia et al., 2019; Maia and Brunelli, 2020) also reveal the presence of large amounts of mylonitic peridotites along the transform (Fig. 1b), representing a high shear stress regime. The axial domain close to the RTI corresponds to an area where mantle-derived peridotites are widely exhumed, similar to what is observed along the amagmatic segments at slow and ultraslow spreading mid-ocean ridges (Cannat et al., 2006; Dick et al., 2003; Michael et al., 2003). Further southward of the RTI, the axial domain is complex, including an oblique non-transform discontinuity, a short MAR segment, another non-transform discontinuity, and another MAR segment (Fig. 1b). Further south, the axial valley along the MAR is well developed up to the Chain transform fault, indicating a robust magmatic segment (Harmon et al., 2018). The collected rock samples along the non-transform discontinuity and MAR are mostly basalts (Fig. 1b) (Bonatti et al., 2001, 1996; Maia and Brunelli, 2020), and they have high water content (Ligi et al., 2005), which could be due to the deep hydration and thinning of the lithosphere along the transform fault, and subsequent mixing with the MAR melt (Wang et al., 2022).

3. Data and Methods

We used seismic data collected during the SMARTIES cruise (Maia et al., 2019), where 19 ocean bottom seismometers (OBSs) were deployed in July-August 2019 for ~21 days (Fig. 1b). We used 514 recorded and well-located earthquakes (Yu et al., 2022) to do seismic travel-time tomography, of which 197 events are located along the Romanche transform fault and 317 events along the MAR (Fig. 2).

All earthquakes were recorded by more than 5 OBSs, located iteratively by the NonLinLoc program (Lomax et al., 2000), and relocated by the HypoDD program (Waldhauser and Ellsworth, 2000). The average horizontal and vertical uncertainties are ~2.8 km and ~2.9 km, respectively (Yu et al., 2022). 413 earthquakes have uncertainties less than 5 km and 101 earthquakes between 5 km and 10 km (Fig. 2). In the inversion, the arrival times of the 101 events with larger location uncertainties were assigned to half the weight of the arrivals of the 413 events. The initial one-dimensional (1-D) model was derived from an active-source seismic refraction profile (Wang et al., 2022), and used for the earthquake location (Yu et al., 2022) (Supporting Information Fig. S1). We then used the VELEST program (Kissling et al., 1994) to calculate the 'Minimum 1-D velocity model'. We constructed a sub-dataset of 360 earthquakes, each of which has arrivals ≥6 and a station GAP of ≤180°, to search for the best-fitting 1-D P-wave velocity model in the VELEST program (Supporting Information Fig. S1). The 1-D S-wave velocity model was calculated using a constant Vp/Vs ratio of 1.73 from the Wadati diagram (Yu et al., 2022).

We set up a 3-D grid with a lateral-grid interval of 10 km and at depths of 0, 3, 6, 8, 9, 10, 11, 12, 13, 14, 15, 18, and 21 km in the study volume. We set the seafloor with an average depth of 4 km to 0 km in the model space. The difference between the true depth and the reference depth is taken into account in the ray tracing. We used a tomographic method (Zhao et al., 1992) to determine 3-D Vp and Vs models and Vp/Vs ratios of the crust and upper mantle beneath the study region. Velocity perturbations at every grid node from a starting model were taken as unknown parameters. We calculated the velocity perturbation in the model by linearly interpolating the velocity perturbations at the eight neighbouring grid nodes. We used an efficient 3-D ray-tracing technique (Zhao et al., 1992) to calculate theoretical travel times and ray paths accurately (Fig. 2). The P-wave and S-wave ray density distributions are shown in Supporting Information Figs. S2 and S3, which indicate that the transform fault and RTI region are well covered by the rays.

To obtain the optimal 3-D grid, we conducted numerous tomographic inversion tests to compute tradeoff curves to obtain the best-fitting damping parameters for Vp and Vs models (Fig. 3). In the inversion, the hypocenter parameters were updated using the inverted 3-D velocity model. The arrivals with travel-time residuals larger than 1 s were neglected because over 90% of the residuals are less than 1.0 s (Fig. 4). The LSQR algorithm (Paige and Saunders, 1982) is used to solve the large but sparse system of equations. The root-mean-square travel-time residuals before and after the inversion are 0.162 s and 0.118 s for the P wave tomography and 0.196 s and 0.152 s for the S wave tomography, respectively, with a variance reduction of 68% and 63%, respectively.

We conducted extensive checkerboard resolution tests (Zhao et al., 1992) to assess the reliability of the resulting tomographic models (Figs. 5 and 6, Supporting Information Figs. S4-S7). To make a checkerboard resolution test, velocity perturbations of ±4% are assigned alternately to the 3-D grid nodes with a node spacing of 10 km at different depth layers. Then theoretical travel times for the synthetic checkerboard model were calculated, which were inverted to obtain an output model. Finally, we checked whether the input checkerboard model could be recovered or not. To simulate the picking errors, we added random noises (-0.1 to +0.1 s) with a standard deviation of 0.1 s to the synthetic travel times before the inversion. Our resolution tests indicate that the 3-D velocity model has a resolution of ~10 km in the lateral direction and 3 km in depth (Figs. 5 and 6, Supporting Information Figs. S4-S7). It should be noticed that we have limited resolution in the upper 3-4 km due to the small number of earthquakes at this depth range. In addition, the relatively large space of OBS stations (20-30 km) also reduces the resolution on the lateral scale. But the resolution tests show that our seismic tomography could resolve the velocity anomalies with a lateral scale of 10 km (Figs. 5 and 6, Supporting Information Figs. S4-S7). Thus, we will discuss the anomalies larger than 10 km laterally and 3 km in depth.

The main features of velocity anomalies beneath the Romanche transform fault, RTI, and MAR axis at depths shallower than 15 km can be well recovered, suggesting that those features are quite reliable and robust. However, for the depth layers greater than 15 km, only the checkboard pattern beneath the transform fault at the longitude east of 17°W can be well recovered (Figs. 5 and 6, Supporting Information Figs. S4-S7) because deep earthquakes (>15 km) occurred there (Fig. 2). Thus, in the following, we will just focus on the velocity model at depths shallower than 15 km (Fig. 7).

4. Results

After the Vp and Vs tomography are determined separately, Vp/Vs ratio images are also obtained (Fig. 7, Supporting Information Figs. S8-S10). The main features of Vp and Vs tomography are similar to each other, but strong lateral heterogeneities are revealed in the shallow lithosphere along the Romanche transform fault (Fig. 7, Supporting Information Figs. S8-S10).

4.1 Along the Romanche transform fault

At shallow depths (<8 km), high Vp and Vs values are observed in the south of the Romanche transform fault (cross-sections AA′—distance 50-100 km, CC′—distance 20-40 km, and DD′—distance 10-40 km in Fig. 7, Supporting Information Figs. S8-S10), in agreement with the high-velocity anomalies revealed by the seismic refraction studies (Gregory et al., 2021; Wang et al., 2022; Wang and Singh, 2022) and are suggestive of the presence of mantle peridotites (serpentinite) near the

seafloor, consistent with extensive seafloor exposure of mantle rocks (Fig. 1b). However, low Vp but high Vs anomalies are revealed along the transform valley at the longitude between 17.6° and 17.3°W (cross-sections AA′—distance 10-30 km and BB′—distance 0-20 km, Fig. 7). Normal to low Vp and Vs values are observed beneath the oceanic core complex on the outside corner (cross-sections AA′—distance 70-90 km in Fig. 7, Supporting Information Figs. S8-S10). At depths of 8-15 km, low Vp and Vs anomalies are widely observed along the transform fault (cross-section AA′—distance 10-100 km in Fig. 7, Supporting Information Figs. S8-S10).

The high Vp/Vs ratios, ~1.8-1.95, are only observed at depths shallower than 10 km around an oblique hill west of RTI (cross-sections AA′—distance 30-50 km and CC′—distance 0-20 km in Fig. 7g). This oblique bathymetric high is identified as a fossil detachment (Maia and Brunelli, 2020) (DF1 in Fig. 7a) where highly altered mylonitic and ultra-mylonitic peridotites were observed (Fig. 1b) (Maia et al., 2019; Maia and Brunelli, 2020). We observed low Vp/Vs ratios (~1.6-1.7) along the Romanche transform fault between 17.6° and 17.3°W (Fig. 7g and 7h), with low Vp and high Vs values (cross-sections AA′ and BB′ in Fig. 7). Most earthquakes at depths shallower than 15 km occurred in the low to normal Vp/Vs ratio region (~1.6-1.7) (Fig. 7g). We compared the ratio of the arrival times of P-wave (t_p) and S-wave (t_s), $(t_s-t_p)/t_p$, for earthquake hypocenters at different OBS stations (Supporting Information Fig. S11), which reflects directly the Vp/Vs ratios (Haberland et al., 2009). We find that they are consistent with the observed Vp/Vs ratios from the seismic tomographic results. Ray paths from the events along the Romanche transform fault at OBS stations (03-06, 09-10) show more low values of $(t_s-t_p)/t_p$ (<0.6) than those at these stations along the MAR (OBS 01, 16-19) (Supporting Information Fig. S11). This indicates that the low Vp/Vs ratios are robust features.

4.2 Along the Mid-Atlantic Ridge

High Vp and Vs anomalies are revealed at shallow depths (<5 km) along the aseismic non-transform discontinuity close to the RTI and beneath the ridge axis (cross-section EE′ in Fig. 7, Supporting Information Figs. S8-S10). Beneath the non-transform discontinuity between 20 and 30 km distance (cross-section EE′ in Fig. 7), low Vp and low Vs values are observed. At deeper depths (5-15 km), normal to low Vp and low Vs values are also determined along the non-transform discontinuity and MAR (cross-section EE′ in Fig. 7).

Low to normal Vp/Vs ratios of 1.6-1.75 (Fig. 7g and 7i) are widely observed at depths of 0-15 km along the ridge axis (cross-section EE′ in Fig. 7). Most microearthquakes beneath the MAR occur in the low to normal Vp/Vs ratios (~1.6-1.7) (Fig. 7g).

5 Discussion

Our results provide large-scale Vp, Vs, and Vp/Vs ratios along ~100 km of the Romanche transform fault and fracture zone, and ~40 km of the MAR system. An increase or decrease in these values from the reference values provides insight into the lithology and dynamic processes responsible for their formation and evolution.

5.1 Serpentinization versus magmatic process

High Vp/Vs ratios, ~1.8-1.95, along with low Vp and Vs anomalies are observed on the west side of the RTI, north of the first oblique hill, at depths of 0-8 km (cross-section CC′—distance 0-20 km in Fig. 7). Laboratory experiments suggest that the serpentinites in the crust and mantle exhibit high Vp/Vs ratios (~1.9-2.2) (Christensen, 2004, 1996). The rock samples collected on this oblique hill were strongly serpentinized peridotites (Maia and Brunelli, 2020) (Fig. 1b, DF1 in Fig. 7). Therefore, we suggest that the high Vp/Vs ratios associated with this hill are due to the serpentinization of peridotites.

In contrast, further west, we observe low Vp, high Vs, and low Vp/Vs ratios at depths of ~0-8 km along the transform fault (cross-sections AA′—distance 10-30 km and BB′—distance 0-20 km, Fig. 7), similar to what has been reported along the Gofar transform fault (Guo et al., 2018; Liu et al., 2023). Previous studies indicate that serpentinization by hydrothermal circulation would increase as the lithosphere ages (Roland et al., 2012, 2010). However, the absence of high Vp/Vs ratios here suggests that the lithosphere is not highly serpentinized, and may consist of mafic rocks. Based on the seismic refraction study across the Romanche transform fault, Gregory et al. (2021) found a ~6-km-thick gabbroic crust, supporting the above hypothesis.

Along the Romanche transform fault, the 2016 M_w 7.1 earthquake occurred at ~20 km depth at 17.83° W (Hicks et al., 2020) (Fig. 1b), and has two-phase rupture processes: i.e., eastward propagation towards the RTI and reversed propagation with super-shear rupture to the west (Hicks et al., 2020). Our observed serpentinized lithosphere near the fossil fragment of detachment faults (DF1 in Fig. 7), with weak slip, appears to support the presence of the rupture barrier near the RTI for the 2016 M_w 7.1 earthquake (Hicks et al., 2020; Yu et al., 2021), which possibly led to the reversing of rupture propagation towards the west (Hicks et al., 2020); whereas the low Vp/Vs ratios along the transform fault (cross-section AA′—distance 10-30 km in Fig. 7) indicate gabbroic materials (Gregory et al., 2021) in the shallow section allowing the super-shear rupture (Hicks et al., 2020).

Beneath the MAR, we did not observe low P-wave and S-wave velocity anomalies beneath the ridge axis at shallow depths (cross-section EE′ in Fig. 7), suggesting weak hydrothermal circulations here.

In contrast, the presence of volcanic features on the seafloor, confirmed by the basalts recovered from the dives (Maia et al., 2019; Maia and Brunelli, 2020) (Fig. 1b), and the low-velocity anomalies in the mantle (cross-section EE′ in Fig. 7) suggest that magmatic processes dominate along the MAR axis.

5.2 Low Vp/Vs ratios

The low Vp/Vs ratios (~1.6-1.7) in the lithosphere on the western portion of the Romanche transform fault (cross-sections AA′—distance 10-30 km and BB′—distance 0-20 km, Fig. 7) are surprising, and are inconsistent with the extensive observation of serpentinized peridotites on the seafloor (Bonatti et al., 2001, 1996; Maia and Brunelli, 2020) that have high Vp/Vs ratios (~1.9-2.2) (Christensen, 2004; Grevemeyer et al., 2018). We analyzed the velocities in the hypocenter region of microearthquakes and found that most mantle earthquakes occurred in the region with low Vp/Vs ratios (~1.6-1.65) (Fig. 8a, Supporting Information Fig. S12). The shallow events beneath the oceanic core complex occur in the region of normal to low Vp/Vs ratios (1.65-1.7) (Fig. 8a).

One possible explanation for the low Vp/Vs ratios is the presence of gas (e.g., carbon dioxide and methane) in the lithosphere that reduces the Vp/Vs ratios, which would lead to a substantial decrease of Vp (the bulk modulus) but only a small decrease of Vs (the shear modulus) (Ito et al., 1979; Wang and Nur, 1989). We used the differential effective medium model (Taylor and Singh, 2002) to estimate the effects of the presence of gas and seawater as well as crack aspect ratios on the seismic velocities of the peridotite in the mantle (Fig. 8b, Supporting Information Fig. S13). The lithological components for the peridotite used in the computation are 61.3% olivine (90% Fo, 10% Fa), 17.4% orthopyroxene (90% En, 10% Fs), 10.8% clinopyroxene (Di), 1.5% spinel, and 9% plagioclase (90% An, 10% Ab), which are obtained by averaging the components of the Romanche transform fault peridotites (site G96) (Tartarotti et al., 2002), except one with a low component of olivine. P- and S-wave speeds for the peridotite were estimated using an Excel tool (Abers and Hacker, 2016). The gas parameters were extracted from Batzle and Wang (1992). Figure 8b shows that Vp/Vs ratios are always higher than 1.7 for the water saturation for all aspect ratios although the ratios can decrease with spherical inclusions (r=1). In contrast, gas saturation can dramatically reduce Vp/Vs ratios, especially for small aspect ratios (r$\geqslant$20) (Fig. 8, Supporting Information Fig. S13), and only 0.5% of gas saturation can explain the resulting Vp/Vs ratios of 1.6-1.7 for an aspect ratio of 50 (thin crack) (Fig. 8b). If this is true, there are two possible mechanisms for the gas source: (1) Dilatancy within the transform fault, in the long run, can cause a decrease of pore pressure, possibly leading to the transition from liquid to vapour (Géli et al., 2014); (2) Serpentinization in the peridotite-hosted oceanic lithosphere at temperatures less than 400-500°C could produce abiogenic gas (methane and hydrogen) (Allen and Seyfried, 2003; Klein

et al., 2019). However, the dilatancy mechanism can only be applicable to short-offset transforms with young lithospheres across the transform, e.g., the Gofar transform fault, where strong hydrothermal fluids participate in the hot crust at shallow depths (Géli et al., 2014). In addition, the serpentinization mechanism cannot account for the low ratios in the deep mantle (>7 km) where the temperature (>500°C) is too high to support peridotite serpentinization (Evans, 2004; Schwartz et al., 2013). Furthermore, it would be difficult to have carbon dioxide or methane in vapour phase under high-pressure and high-temperature conditions. Thus, the gas possibility can only explain the low ratios at shallow depths (<7 km) with low temperatures (<500°C) where the peridotite is prevailing and its serpentinization is able to occur and release gas (Allen and Seyfried, 2003; Klein et al., 2019).

Previous studies have indicated that the thick cracks (spherical pores) (Brantut and David, 2019; Kim et al., 2019; Takei, 2002) can lead to the reduction of Vp/Vs ratios. Fluid saturation at low pressures can also lead to low Vp/ Vs ratios (Spencer and Nur, 1976). The thick and wide cracks in the crust at mid-ocean ridges, resulting from the extensional stress, can allow long-lived hydrothermal circulation (Kim et al., 2019). The focal mechanism solutions have indicated some extensional stresses along the Romanche transform fault (Yu et al., 2022, 2021), which likely supports the presence of thick and wide cracks. This mechanism can only explain the observed low Vp/Vs ratios at shallow depths (<7 km). However, in our study area, the low Vp/Vs anomalies extend down to 15 km (Fig. 7), where the pressure is too high to support the presence of long-lived thick cracks.

The reduction in Vp/Vs ratios can also be attributed to the rock compositions. The abundance of quartz can decrease Vp/Vs ratios, leading to low Vp and high Vs (Christensen, 1996; Powell et al., 2010), which is consistent with our observations along the transform fault (cross-sections AA′—distance 10-30 km and BB′—distance 0-20 km, in Fig. 7). However, our rock samplings have no evidence for high components of quartz (Fig. 1b) (Maia et al., 2019). Recent studies indicate that orthopyroxene enrichment in the peridotites will dramatically decrease the Vp/Vs ratios in the mantle wedge (Hacker and Abers, 2012; Qian et al., 2018; Wagner et al., 2008) (Fig. 8c). Preliminary on-board study on the dive samples collected during the SMARTIES experiment indicated that high components of orthopyroxene and low proportions of olivine are present along the eastern end of the Romanche transform, with an average value of orthopyroxene of 20-40%, reaching as high as >70% in some samples (Maia et al., 2019). This is much higher than those found in the middle and western Romanche transform fault (Tartarotti et al., 2002). Pure orthopyroxene at elevated temperature (~900°C) can have very low Vp/Vs ratios, ~1.5-1.6 (Fig. 8c) (Jackson et al., 2007). But when high pressure is considered, the Vs and Vp/Vs ratios will increase (Fig. 8c) (Hacker and Abers, 2012; Qian et al., 2018). It should be noted that our unusual observations of low Vp/Vs ratios are located at depths shallower than 15 km,

where the pressure is much lower than that in the mantle wedge (50-150 km). At shallower depths, the S-wave velocity will be lower than that suggested by computations in the mantle wedge (Hacker and Abers, 2012; Qian et al., 2018), and would better match our low-ratio patterns for the earthquakes along the Romanche transform fault (Fig. 8c). The orthopyroxene abundance can result from extensive water-rock interactions in the lithosphere (Smith et al., 1999). A recent tomography study indicates that mantle hydration beneath the Romanche transform fault can occur as deep as 32 km (Wang et al., 2022), which seems to support this hypothesis. The presence of orthopyroxene enrichment down to 15 km depth might also explain the rupture initiation at 16 km for the 2016 M_w 7.1 earthquake (Hicks et al., 2020). Orthopyroxene would have a weakening effect (Farla et al., 2013), allowing it to accommodate stress at these depths, and hence causing rupture failure.

Similar low Vp/Vs ratios (~1.61-1.69) have also been found below the rupture area along the Gofar transform faults, which is attributed to the metamorphic minerals (Liu et al., 2023). To produce orthopyroxene-rich peridotites, a significant quantity of silica is needed in the mantle. Hauri *et al.* (2018) suggested that there are recycled subduction zone materials in the mantle of the equatorial Atlantic Ocean, which were imported as the Atlantic Ocean opened during the ancient Iapetus Ocean. The ancient and recycled subduction materials can be responsible for the silica abundance necessary to crystallise orthopyroxene in the mantle, leading to the low Vp/Vs ratios along the transform fault. However, this explanation cannot explain the low Vp/Vs ratios in the RTI where the velocities are slow (Fig. 8c), but the anomaly is narrow.

Seismic anisotropy, mostly resulting from the crystal-preferred orientation of minerals, also affects the Vp/Vs ratio. The crystal-preferred orientation of olivine can lead to high Vp/Vs ratios (Christensen, 2004). In contrast, both studies of chlorite and orthopyroxene indicate higher Vs anisotropy than Vp anisotropy, which can reduce Vp/Vs ratios (Jackson et al., 2007; Kim and Jung, 2015; Mookherjee and Mainprice, 2014). In addition, Figure 8d shows that the velocity can be significantly changed by the angle between the wave propagation with the preferred plane of minerals. For the metasomatized minerals, e.g., chlorite (Mookherjee and Mainprice, 2014) and amphibole (Ji et al., 2013), anisotropic velocities for P and S waves along some propagating directions could contribute to some of the low ratios we observe (Fig. 8d) (1.60-1.65), which have higher S-wave velocities than the values caused by orthopyroxene enrichment (Fig. 8c). In the study region, large amounts of mylonitic peridotites along the transform fault and fracture zone are observed (Fig. 1b) (Maia et al., 2019; Maia and Brunelli, 2020; Yu et al., 2021), and we can expect similar chlorite and amphibole compositions as those deformed peridotites observed at the Southwest Indian Ridge (Kohli et al., 2021; Prigent et al., 2020). Furthermore, in the Chain RTI, ~200 km south of our study area, a very recent seismic study indicates

ridge-parallel anisotropy near the ridge axis caused by sub-vertical melt alignment and spreading-parallel anisotropy away from the ridge axis produced by plate motions (Kendall et al., 2023). The spreading-parallel fabric in the mantle could lead to fast S-wave velocity along the transform, which may lead to the low Vp/Vs ratios we observed. The presence of vertically aligned melt beneath the ridge axis (Kendall et al., 2023) also affects the Vp/Vs ratios. Therefore, the seismic anisotropy for low Vp/Vs ratios cannot be ruled out but more seismic and geological evidence is required.

6 Conclusions

Using travel-time data of 514 microearthquakes recorded by a temporary network of OBSs, we present the detailed structure of the crust and mantle around the eastern Romanche transform fault, RTI, and MAR. High Vp/Vs ratios (~1.8-1.95) are only mapped north of the first oblique hill juxtaposed with the RTI, indicating strong peridotite serpentinization, which is supported by altered peridotite samples collected on the seafloor. This serpentinized region has also acted as a rupture barrier for the 2016 M_w 7.1 large earthquake. Low Vp/Vs ratios (~1.6-1.7) are observed along the western portion of the Romanche transform fault, which could be explained by the presence of thick and wide cracks at shallow depths of 0-8 km and orthopyroxene enrichment at depths of 8-15 km, allowing the rupture initiation at 16 km and super-shear in the shallow lithosphere for the 2016 M_w 7.1 large earthquake. Beneath the MAR axis, Vp/Vs ratios are mostly ~1.7, indicating the absence of serpentinization in the mantle, and hence suggesting that magmatism is the dominant process at the ridge axis

CRediT authorship contribution statement

Zhiteng Yu: Conceptualization, Formal analysis, Investigation, Methodology, Visualization, Writing - Original Draft.

Satish C. Singh: Funding acquisition, Software, Supervision, Writing - Review & Editing.

Marcia Maia: Funding acquisition, Supervision, Project administration, Writing - Review & Editing.

Declaration of competing interest

The authors declare that they have no known competing financial interests or personal relationships that could have appeared to influence the work reported in this paper.

Data Availability Statement

Raw seismic data and the cruise report can be requested from the website

(https://campagnes.flotteoceanographique.fr/campagnes/18001107/). The figures were plotted using the Generic Mapping Tools (https://github.com/GenericMappingTools/gmt/releases/tag/6.3.0).

Acknowledgements

We thank the officers, crew, and scientific technicians of the 2019 SMARTIES cruise for their hard work. We thank L. Géli and D. Brunelli for their useful discussions. We further thank Prof. Hans Thybo (the Editor) and anonymous reviewers for valuable comments and suggestions that improved this manuscript. This research was funded the ISblue project, the Interdisciplinary graduate school for the blue planet (ANR-17-EURE-0015, ZY, MM), the French government under the program "Investissements d'Avenir" (ZY, MM), the Regional Council of Brittany (SAD programme) (ZY), the Programme Tellus INSU " Campagnes à la Mer" (MM), the European Research Council under the European Union's Seventh Framework Programme (FP7/2007–2013) (SS), and the European Research Council Advance Grant agreement no. 339442_TransAtlanticILAB (SS). The ship time for the SMARTIES cruise was funded through the TGIR French Oceanographic Fleet (MM). This work is IPGP contribution no. XXX.

Appendix A. Supplementary material

Supplementary information is available for this article. Correspondence and requests for materials should be addressed to Zhiteng Yu. The 3-D velocity models are available on the Zenodo dataset repository (https://doi.org/10.5281/zenodo.7856306).

References

Abers, G.A., Hacker, B.R., 2016. A MATLAB toolbox and Excel workbook for calculating the densities, seismic wave speeds, and major element composition of minerals and rocks at pressure and temperature. Geochem. Geophys. Geosystems 17, 616–624. https://doi.org/10.1002/2015gc006171

Allen, D.E., Seyfried, W.E., 2003. Compositional controls on vent fluids from ultramafic-hosted hydrothermal systems at mid-ocean ridges: An experimental study at 400° C, 500 bars. Geochim. Cosmochim. Acta 67, 1531–1542. https://doi.org/10.1016/s0016-7037(02)01173-0

Batzle, M., Wang, Z., 1992. Seismic properties of pore fluids. Geophysics 57, 1396–1408. https://doi.org/10.1190/1.1443207

Becker, K., Sakai, H., et al. (Eds.), 1989. Proceedings of the Ocean Drilling Program, 111 Scientific Reports, Proceedings of the Ocean Drilling Program. Ocean Drilling Program. https://doi.org/10.2973/odp.proc.sr.111.1989

Bonatti, E., Brunelli, D., Fabretti, P., Ligi, M., Portaro, R.A., Seyler, M., 2001. Steady-state creation of crust-free lithosphere at cold spots in mid-ocean ridges. Geology

979–982. https://doi.org/10.1130/0091-7613(2001)029<0979:sscocf>2.0.co;2

Bonatti, E., Ligi, M., Carrara, G., Gasperini, L., Turko, N., Perfiliev, S., Peyve, A., Sciuto, P.F., 1996. Diffuse impact of the Mid-Atlantic Ridge with the Romanche transform: an ultracold ridge-transform intersection. J. Geophys. Res. Solid Earth 101, 8043–8054. https://doi.org/10.1029/95jb02249

Bonatti, E., Ligi, M., Gasperini, L., Peyve, A., Raznitsin, Y., Chen, Y.J., 1994. Transform migration and vertical tectonics at the Romanche fracture zone, equatorial Atlantic. J. Geophys. Res. Solid Earth 99, 21779–21802. https://doi.org/10.1029/94jb01178

Brantut, N., David, E.C., 2019. Influence of fluids on VP/VS ratio: increase or decrease? Geophys. J. Int. 216, 2037–2043. https://doi.org/10.1093/gji/ggy518

Cannat, M., Sauter, D., Ruellan, E., Okino, K., Escartin, J., Combier, V., Baala, M., 2006. Modes of seafloor generation at a melt-poor ultraslow-spreading ridge 5.

Christensen, N.I., 2004. Serpentinites, Peridotites, and Seismology. Int. Geol. Rev. 46, 795–816. https://doi.org/10.2747/0020-6814.46.9.795

Christensen, N.I., 1996. Poisson's ratio and crustal seismology. J. Geophys. Res. Solid Earth 101, 3139–3156. https://doi.org/10.1029/95jb03446

DeMets, C., Gordon, R.G., Argus, D.F., 2010. Geologically current plate motions. Geophys. J. Int. 181, 1–80. https://doi.org/10.1111/j.1365-246x.2009.04491.x

Detrick, R.S., White, R.S., Purdy, G.M., 1993. Crustal structure of North Atlantic Fracture Zones. Rev. Geophys. 31, 439. https://doi.org/10.1029/93rg01952

Dick, H.J.B., Lin, J., Schouten, H., 2003. An ultraslow-spreading class of ocean ridge. Nature 426, 405–412. https://doi.org/10.1038/nature02128

Evans, B.W., 2004. The Serpentinite Multisystem Revisited: Chrysotile Is Metastable. Int. Geol. Rev. 46, 479–506. https://doi.org/10.2747/0020-6814.46.6.479

Farla, R.J.M., Karato, S., Cai, Z., 2013. Role of orthopyroxene in rheological weakening of the lithosphere via dynamic recrystallization. Proc. Natl. Acad. Sci. 110, 16355–16360. https://doi.org/10.1073/pnas.1218335110

Géli, L., Piau, J.-M., Dziak, R., Maury, V., Fitzenz, D., Coutellier, Q., Henry, P., Broseta, D., Steele-MacInnis, M., Driesner, T., 2014. Seismic precursors linked to highly compressible fluids at oceanic transform faults. Nat. Geosci. 7, 757–761. https://doi.org/10.1038/ngeo2244

Gregory, E.P.M., Singh, S.C., Marjanović, M., Wang, Z., 2021. Serpentinized peridotite versus thick mafic crust at the Romanche oceanic transform fault. Geology 49, 1132–1136. https://doi.org/10.1130/g49097.1

Grevemeyer, I., Hayman, N.W., Peirce, C., Schwardt, M., Van Avendonk, H.J.A., Dannowski, A., Papenberg, C., 2018. Episodic magmatism and serpentinized mantle exhumation at an ultraslow-spreading centre. Nat. Geosci. 11, 444–448. https://doi.org/10.1038/s41561-018-0124-6

Grevemeyer, I., Rüpke, L.H., Morgan, J.P., Iyer, K., Devey, C.W., 2021. Extensional tectonics and two-stage crustal accretion at oceanic transform faults. Nature 591, 402–407. https://doi.org/10.1038/s41586-021-03278-9

Growe, K., Grevemeyer, I., Singh, S.C., Marjanović, M., Gregory, E.P.M., Papenberg, C., Vaddineni, V., Gómez de la Peña, L., Wang, Z., 2021. Seismic Structure of the St. Paul

Fracture Zone and Late Cretaceous to Mid Eocene Oceanic Crust in the Equatorial Atlantic Ocean Near 18° W. J. Geophys. Res. Solid Earth 126. https://doi.org/10.1029/2021jb022456

Guo, H., Zhang, H., Froment, B., 2018. Structural control on earthquake behaviors revealed by high-resolution V_p/V_s imaging along the Gofar transform fault, East Pacific Rise. Earth Planet. Sci. Lett. 499, 243–255. https://doi.org/10.1016/j.epsl.2018.07.037

Haberland, C., Rietbrock, A., Lange, D., Bataille, K., Dahm, T., 2009. Structure of the seismogenic zone of the southcentral Chilean margin revealed by local earthquake traveltime tomography. J. Geophys. Res. Solid Earth 114, 2008JB005802. https://doi.org/10.1029/2008JB005802

Hacker, B.R., Abers, G.A., 2012. Subduction Factory 5: Unusually low Poisson's ratios in subduction zones from elastic anisotropy of peridotite. J. Geophys. Res. Solid Earth 117, B06308. https://doi.org/10.1029/2012jb009187

Hacker, B.R., Abers, G.A., 2004. Subduction Factory 3: An Excel worksheet and macro for calculating the densities, seismic wave speeds, and H $_2$ O contents of minerals and rocks at pressure and temperature: SUBDUCTION FACTORY 3. Geochem. Geophys. Geosystems 5, n/a-n/a. https://doi.org/10.1029/2003gc000614

Harmon, N., Rychert, C., Agius, M., Tharimena, S., Le Bas, T., Kendall, J.M., Constable, S., 2018. Marine Geophysical Investigation of the Chain Fracture Zone in the Equatorial Atlantic From the PI-LAB Experiment. J. Geophys. Res. Solid Earth 123. https://doi.org/10.1029/2018jb015982

Hauri, E.H., Maclennan, J., McKenzie, D., Gronvold, K., Oskarsson, N., Shimizu, N., 2018. CO_2 content beneath northern Iceland and the variability of mantle carbon. Geology 46, 55–58. https://doi.org/10.1130/G39413.1

Hicks, S.P., Okuwaki, R., Steinberg, A., Rychert, C.A., Harmon, N., Abercrombie, R.E., Bogiatzis, P., Schlaphorst, D., Zahradnik, J., Kendall, J.-M., Yagi, Y., Shimizu, K., Sudhaus, H., 2020. Back-propagating supershear rupture in the 2016 M_w 7.1 Romanche transform fault earthquake. Nat. Geosci. 13, 647–653. https://doi.org/10.1038/s41561-020-0619-9

Ito, H., DeVilbiss, J., Nur, A., 1979. Compressional and shear waves in saturated rock during water-steam transition. J. Geophys. Res. Solid Earth 84, 4731–4735. https://doi.org/10.1029/jb084ib09p04731

Jackson, J.M., Sinogeikin, S.V., Bass, J.D., 2007. Sound velocities and single-crystal elasticity of orthoenstatite to 1073K at ambient pressure. Phys. Earth Planet. Inter. 161, 1–12. https://doi.org/10.1016/j.pepi.2006.11.002

Ji, S., Shao, T., Michibayashi, K., Long, C., Wang, Q., Kondo, Y., Zhao, W., Wang, H., Salisbury, M.H., 2013. A new calibration of seismic velocities, anisotropy, fabrics, and elastic moduli of amphibole-rich rocks: SEISMIC PROPERTIES OF AMPHIBOLITES. J. Geophys. Res. Solid Earth 118, 4699–4728. https://doi.org/10.1002/jgrb.50352

Johnston, J.E., Christensen, N.I., 1997. Seismic properties of layer 2 basalts. Geophys. J. Int. 128, 285–300. https://doi.org/10.1111/j.1365-246X.1997.tb01555.x

Kendall, J.M., Schlaphorst, D., Rychert, C.A., Harmon, N., Agius, M., Tharimena, S., 2023. Seismic anisotropy indicates organized melt beneath the Mid-Atlantic Ridge aids seafloor spreading. Geology. https://doi.org/10.1130/G51550.1

Kim, D., Jung, H., 2015. Deformation microstructures of olivine and chlorite in chlorite

peridotites from Almklovdalen in the Western Gneiss Region, southwest Norway, and implications for seismic anisotropy. Int. Geol. Rev. 57, 650–668. https://doi.org/10.1080/00206814.2014.936054

Kim, E., Toomey, D.R., Hooft, E.E.E., Wilcock, W.S.D., Weekly, R.T., Lee, S., Kim, Y.H., 2019. Upper Crustal *Vp*/*Vs* Ratios at the Endeavour Segment, Juan de Fuca Ridge, From Joint Inversion of *P* and *S* Traveltimes: Implications for Hydrothermal Circulation. Geochem. Geophys. Geosystems 20, 208–229. https://doi.org/10.1029/2018gc007921

Kissling, E., Ellsworth, W.L., Eberhart-Phillips, D., Kradolfer, U., 1994. Initial reference models in local earthquake tomography. J. Geophys. Res. Solid Earth 99, 19635–19646. https://doi.org/10.1029/93JB03138

Klein, F., Grozeva, N.G., Seewald, J.S., 2019. Abiotic methane synthesis and serpentinization in olivine-hosted fluid inclusions. Proc. Natl. Acad. Sci. 116, 17666–17672. https://doi.org/10.1073/pnas.1907871116

Kohli, A., Wolfson-Schwehr, M., Prigent, C., Warren, J.M., 2021. Oceanic transform fault seismicity and slip mode influenced by seawater infiltration. Nat. Geosci. 14, 606–611. https://doi.org/10.1038/s41561-021-00778-1

Ligi, M., Bonatti, E., Cipriani, A., Ottolini, L., 2005. Water-rich basalts at mid-ocean-ridge cold spots. Nature 434, 66–69. https://doi.org/10.1038/nature03264

Ligi, M., Cuffaro, M., Chierici, F., Calafato, A., 2008. Three-dimensional passive mantle flow beneath mid-ocean ridges: an analytical approach. Geophys. J. Int. 175, 783–805. https://doi.org/10.1111/j.1365-246x.2008.03931.x

Liu, T., Gong, J., Fan, W., Lin, G., 2023. In-situ V_p/V_s reveals fault-zone material variation at the westernmost Gofar transform fault, East Pacific Rise. J. Geophys. Res. Solid Earth. https://doi.org/10.1029/2022JB025310

Lomax, A., Virieux, J., Volant, P., Berge-Thierry, C., 2000. Probabilistic earthquake location in 3D and layered models, in: Advances in Seismic Event Location. Springer, pp. 101–134.

Maia, M., Brunelli, D., 2020. The Eastern Romanche ridge-transform intersection (Equatorial Atlantic): slow spreading under extreme low mantle temperatures. Preliminary results of the SMARTIES cruise., in: EGU General Assembly Conference Abstracts. p. 10314. https://doi.org/10.5194/egusphere-egu2020-10314

Maia, M., Brunelli, D., Ligi, M., 2019. SMARTIES cruise,Pourquoi pas? R/V. https://doi.org/10.17600/18001107

Marjanović, M., Singh, S.C., Gregory, E.P.M., Grevemeyer, I., Growe, K., Wang, Z., Vaddineni, V., Laurencin, M., Carton, H., Peña, L.G. de la, Filbrandt, C., 2020. Seismic Crustal Structure and Morphotectonic Features Associated With the Chain Fracture Zone and Their Role in the Evolution of the Equatorial Atlantic Region. J. Geophys. Res. Solid Earth 125, e2020JB020275. https://doi.org/10.1029/2020JB020275

Michael, P.J., Langmuir, C.H., Dick, H.J.B., Snow, J.E., Goldstein, S.L., Graham, D.W., Lehnert, K., Kurras, G., Jokat, W., Mühe, R., Edmonds, H.N., 2003. Magmatic and amagmatic seafloor generation at the ultraslow-spreading Gakkel ridge, Arctic Ocean. Nature 423, 956–961. https://doi.org/10.1038/nature01704

Mookherjee, M., Mainprice, D., 2014. Unusually large shear wave anisotropy for chlorite in subduction zone settings. Geophys. Res. Lett. 41, 1506–1513.

https://doi.org/10.1002/2014gl059334

Paige, C.C., Saunders, M.A., 1982. LSQR: An algorithm for sparse linear equations and sparse least squares. ACM Trans. Math. Softw. TOMS 8, 43–71.

Powell, C.A., Withers, M.M., DeShon, H.R., Dunn, M.M., 2010. Intrusions and anomalous Vp/Vs ratios associated with the New Madrid seismic zone. J. Geophys. Res. Solid Earth 115. https://doi.org/10.1029/2009JB007107

Prigent, C., Warren, J.M., Kohli, A.H., Teyssier, C., 2020. Fracture-mediated deep seawater flow and mantle hydration on oceanic transform faults. Earth Planet. Sci. Lett. 532, 115988. https://doi.org/10.1016/j.epsl.2019.115988

Qian, W., Wang, W., Zou, F., Wu, Z., 2018. Elasticity of Orthoenstatite at High Pressure and Temperature: Implications for the Origin of Low V_P/V_S Zones in the Mantle Wedge. Geophys. Res. Lett. 45, 665–673. https://doi.org/10.1002/2017gl075647

Roland, E., Behn, M.D., Hirth, G., 2010. Thermal-mechanical behavior of oceanic transform faults: Implications for the spatial distribution of seismicity. Geochem. Geophys. Geosystems 11, Q07001. https://doi.org/10.1029/2010gc003034

Roland, E., Lizarralde, D., McGuire, J.J., Collins, J.A., 2012. Seismic velocity constraints on the material properties that control earthquake behavior at the Quebrada-Discovery-Gofar transform faults, East Pacific Rise. J. Geophys. Res. Solid Earth 117, B11102. https://doi.org/10.1029/2012jb009422

Schwartz, S., Guillot, S., Reynard, B., Lafay, R., Debret, B., Nicollet, C., Lanari, P., Auzende, A.L., 2013. Pressure–temperature estimates of the lizardite/antigorite transition in high pressure serpentinites. Lithos 178, 197–210. https://doi.org/10.1016/j.lithos.2012.11.023

Smith, D., Alexis Riter, J.C., Mertzman, S.A., 1999. Water–rock interactions, orthopyroxene growth, and Si-enrichment in the mantle: evidence in xenoliths from the Colorado Plateau, southwestern United States. Earth Planet. Sci. Lett. 165, 45–54. https://doi.org/10.1016/s0012-821x(98)00251-9

Spencer, J.W., Nur, A.M., 1976. The effects of pressure, temperature, and pore water on velocities in westerly granite. J. Geophys. Res. 81, 899–904. https://doi.org/10.1029/JB081i005p00899

Takei, Y., 2002. Effect of pore geometry on V_P/V_S: From equilibrium geometry to crack. J. Geophys. Res. 107. https://doi.org/10.1029/2001jb000522

Tartarotti, P., Susini, S., Nimis, P., Ottolini, L., 2002. Melt migration in the upper mantle along the Romanche Fracture Zone (Equatorial Atlantic). Lithos 63, 125–149. https://doi.org/10.1016/s0024-4937(02)00116-0

Taylor, M.A.J., Singh, S.C., 2002. Composition and microstructure of magma bodies from effective medium theory. Geophys. J. Int. 149, 15–21. https://doi.org/10.1046/j.1365-246x.2002.01577.x

Wagner, L.S., Anderson, M.L., Jackson, J.M., Beck, S.L., Zandt, G., 2008. Seismic evidence for orthopyroxene enrichment in the continental lithosphere. Geology 36, 935. https://doi.org/10.1130/g25108a.1

Waldhauser, F., Ellsworth, W.L., 2000. A double-difference earthquake location algorithm: Method and application to the northern Hayward fault, California. Bull. Seismol. Soc. Am. 90, 1353–1368. https://doi.org/10.1785/0120000006

Wang, Z., Nur, A.M., 1989. Effects of CO2 flooding on wave velocities in rocks with hydrocarbons. SPE Reserv. Eng. 4, 429–436. https://doi.org/10.2118/17345-pa

Wang, Z., Singh, S., 2022. Seismic evidence for uniform crustal accretion along slow-spreading ridges in the equatorial Atlantic Ocean (preprint). In Review. https://doi.org/10.21203/rs.3.rs-1366304/v1

Wang, Z., Singh, S.C., Prigent, C., Gregory, E.P.M., Marjanović, M., 2022. Deep hydration and lithospheric thinning at oceanic transform plate boundaries. Nat. Geosci. 15, 741–746. https://doi.org/10.1038/s41561-022-01003-3

Wilson, J.T., 1965. A New Class of Faults and their Bearing on Continental Drift. Nature 207, 343–347. https://doi.org/10.1038/207343a0

Yu, Z., Singh, S., Grenet, L., Maia, M., Hamelin, C., Briais, A., Petracchini, L., Brunelli, D., 2022. CO2 degassing in the mantle triggers deep earthquakes at the Mid-Atlantic Ridge (preprint). In Review. https://doi.org/10.21203/rs.3.rs-1945608/v1

Yu, Z., Singh, S.C., Gregory, E.P.M., Maia, M., Wang, Z., Brunelli, D., 2021. Semibrittle seismic deformation in high-temperature mantle mylonite shear zone along the Romanche transform fault. Sci. Adv. 7, eabf3388. https://doi.org/10.1126/sciadv.abf3388

Zhao, D., Hasegawa, A., Horiuchi, S., 1992. Tomographic imaging of P and S wave velocity structure beneath northeastern Japan. J. Geophys. Res. 97, 19909–19928. https://doi.org/10.1029/92jb00603

Figures

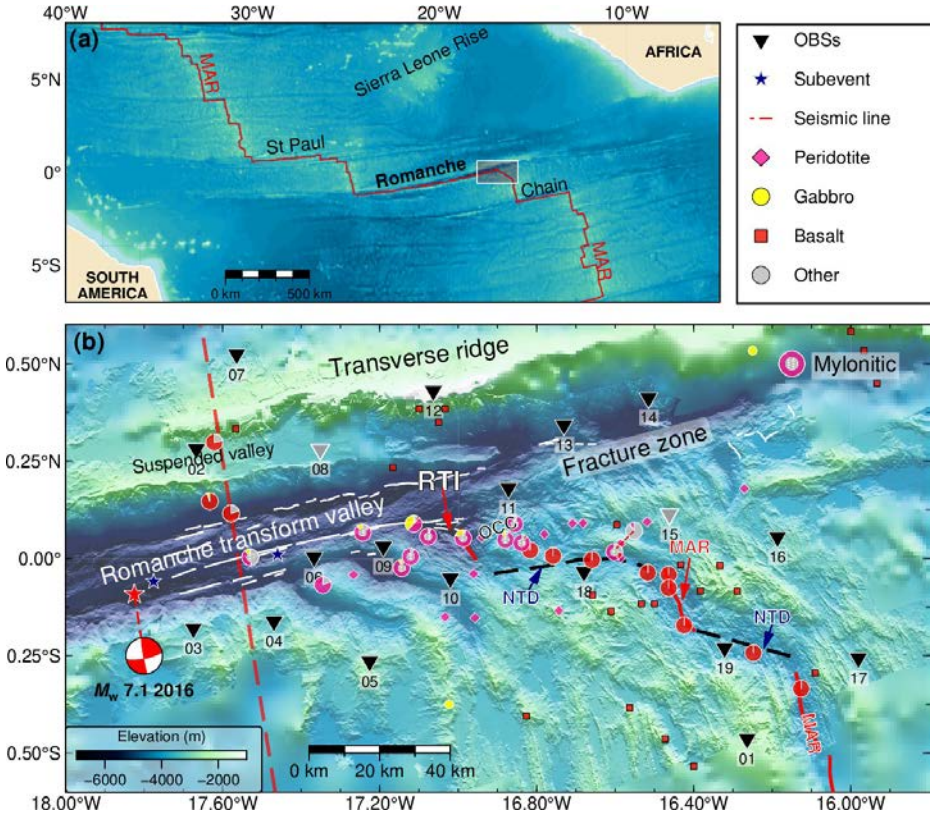

Fig. 1. **Study area.** (**a**) Location of the study region and other major oceanic transform faults in the equatorial Atlantic Ocean. Red lines show the Mid-Atlantic Ridge (MAR) and active transform faults. (**b**) Bathymetric map with petrology in the vicinity of the eastern Romanche transform-ridge intersection (RTI), showing the seismic experiment. The white lines indicate the faults along the transform. Rock samples are shown in coloured symbols (see legends on the right top) (Bonatti et al., 2001, 1996; Maia and Brunelli, 2020). The dashed blue and solid red lines indicate the non-transform discontinuity and MAR, respectively. The triangles are the deployed ocean-bottom seismometers (OBSs) during the SMARTIES cruise (Maia et al., 2019), of which the grey ones were lost or had no data. The red star and blue stars indicate the 2016 M_w 7.1 Romanche earthquake and two subevents, respectively (Hicks et al., 2020). The dashed red line shows the seismic refraction profile (Gregory et al., 2021; Wang et al., 2022). 25 Nautile dives presented in pie charts are from the SMARTIES cruise report (Maia et al., 2019) and mylonitic peridotites are also marked. NTD=Non-transform discontinuity.

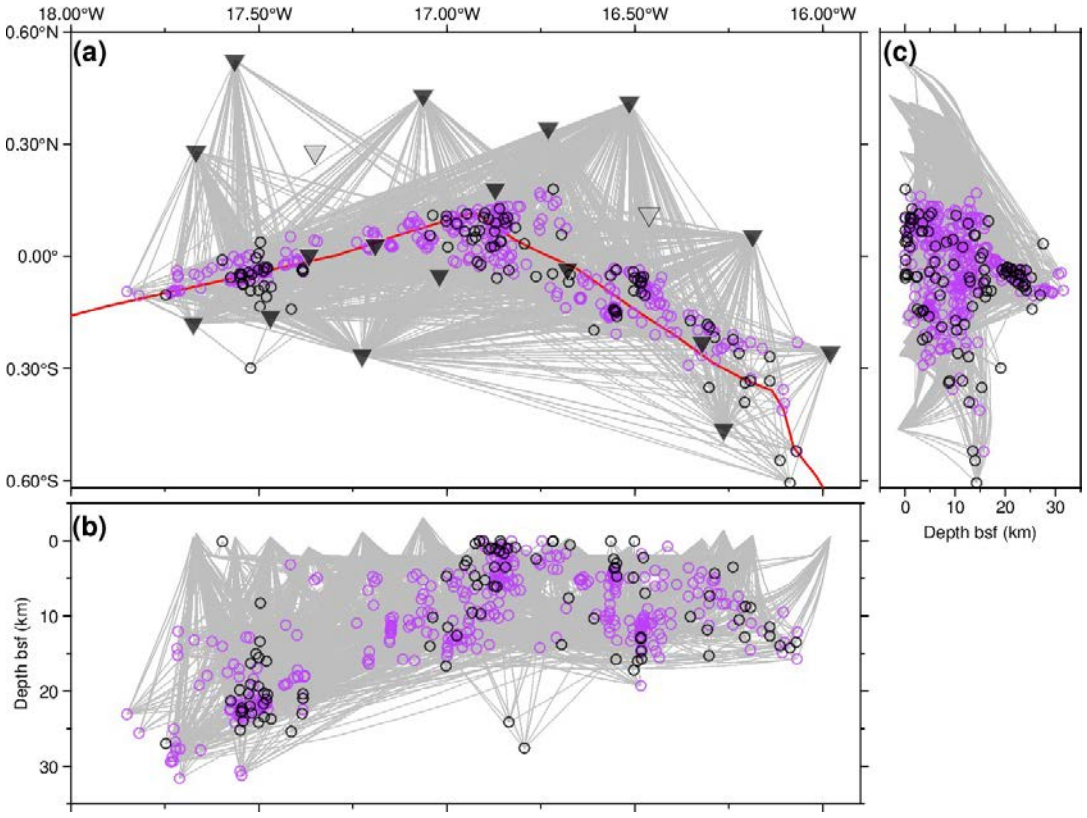

Fig. 2. Ray paths for 514 earthquakes used in seismic tomography. (**a**) Distribution of ray paths (grey lines) from the epicentres (circles) to the OBS stations (triangles). The thick red lines indicate the locations of the MAR and Romanche transform fault. Magenta circles indicate earthquakes with uncertainties less than 5 km, while black ones show earthquakes with uncertainties of 5-10 km. (**b**) East-west and (**c**) north-south vertical cross sections. bsf=below the seafloor.

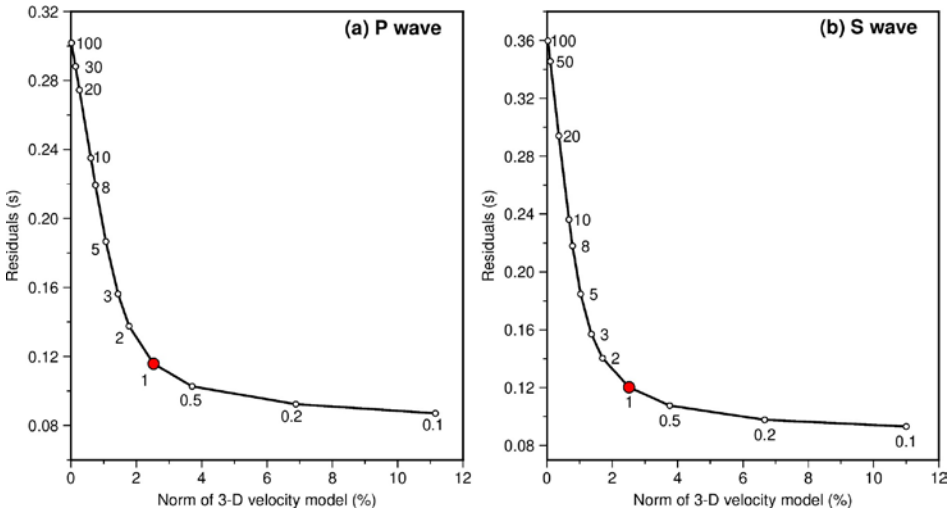

Fig. 3. Trade-off curves for the norm of the P-wave (a) and S-wave (b) velocity models and the RMS travel-time residuals. The red circles indicate the optimal damping parameters for the tomographic models.

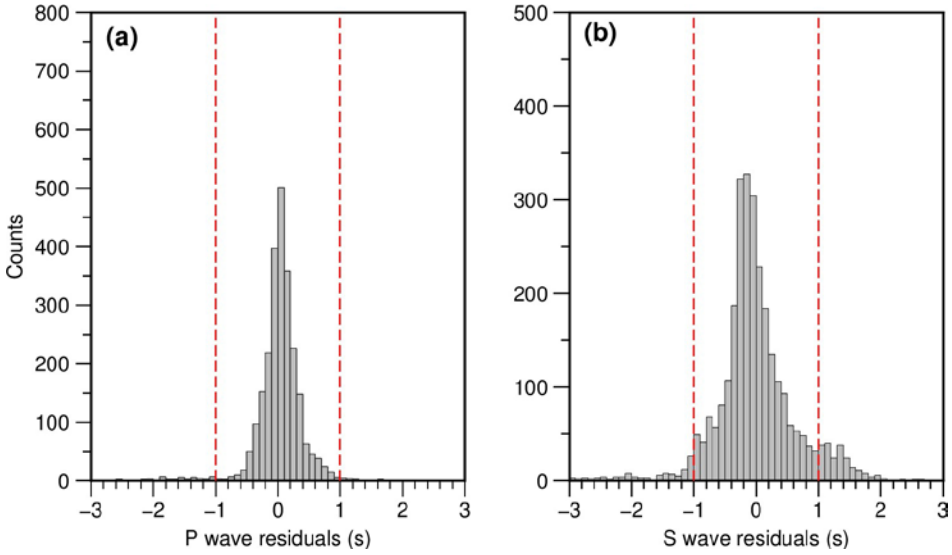

Fig. 4. Histograms of travel-time residuals of the P-wave (a) and S-wave (b) tomography. Arrivals with travel-time residuals larger than 1 s (dashed red lines) were removed in the inversion.

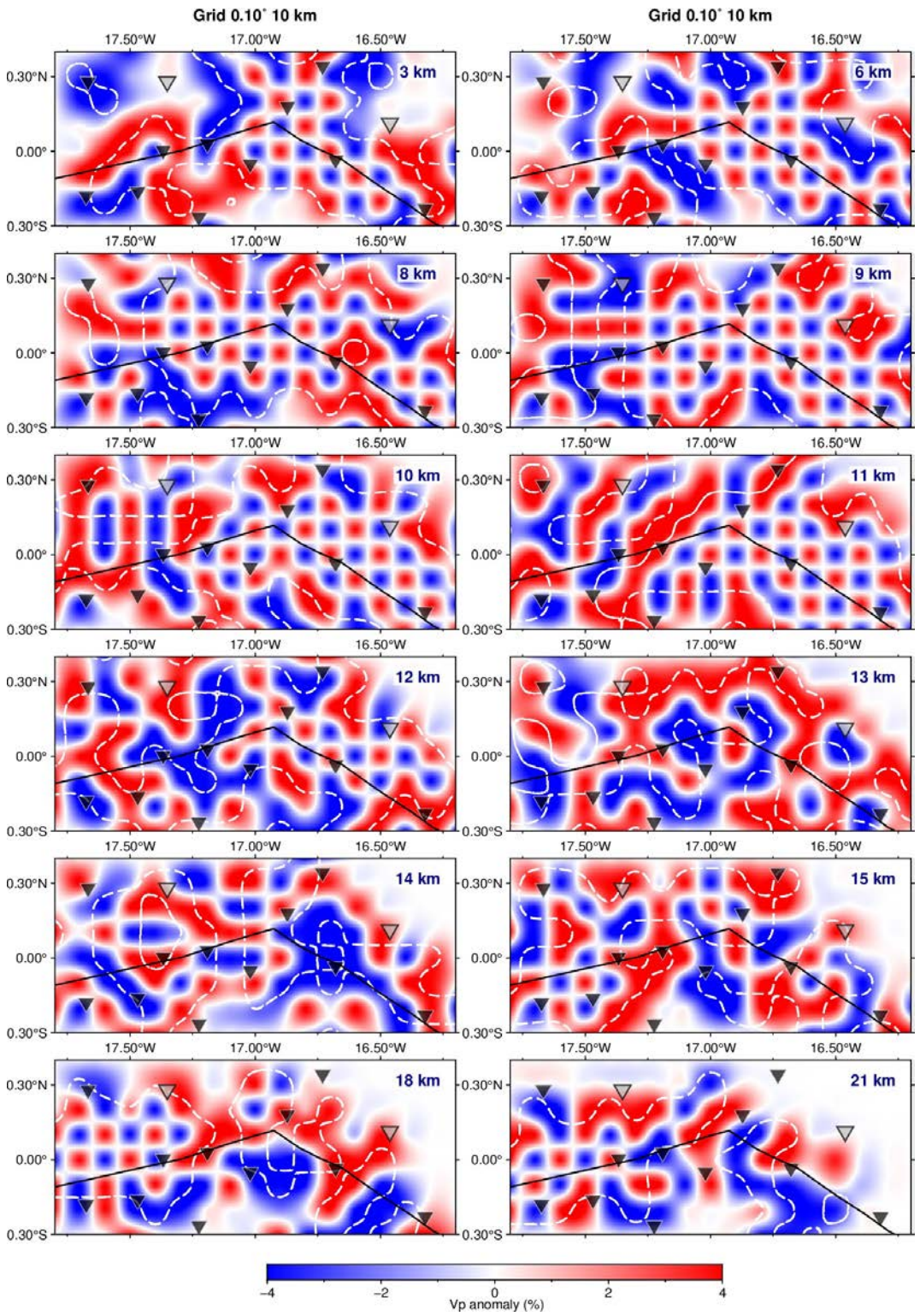

Fig. 5. Results of a checkerboard resolution test for the P-wave tomography. The grid interval is 0.10°, ~10 km. The input amplitudes of the velocity perturbations are ±4%, whose scale is shown at the bottom. The layer depth is shown in the top right corner of each map. The thick white dashed lines indicate that the restored amplitudes are greater than 60%. The black lines indicate the locations of the Romanche transform

fault and MAR. The other labelling is the same as that in Fig. 1.

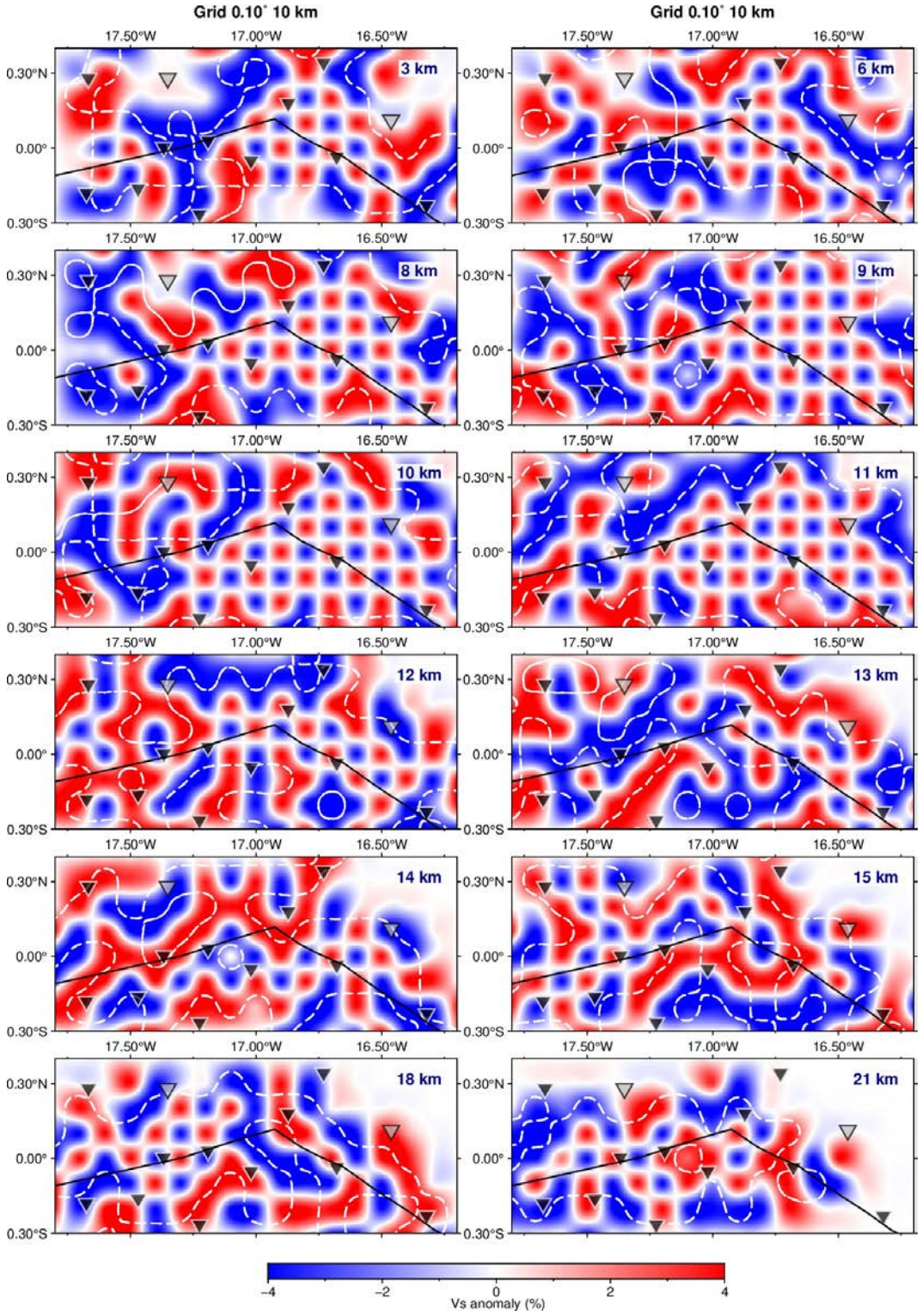

Fig. 6. Results of a checkerboard resolution test for the S-wave tomography. The same as Fig. 5 but for the S-wave tomography.

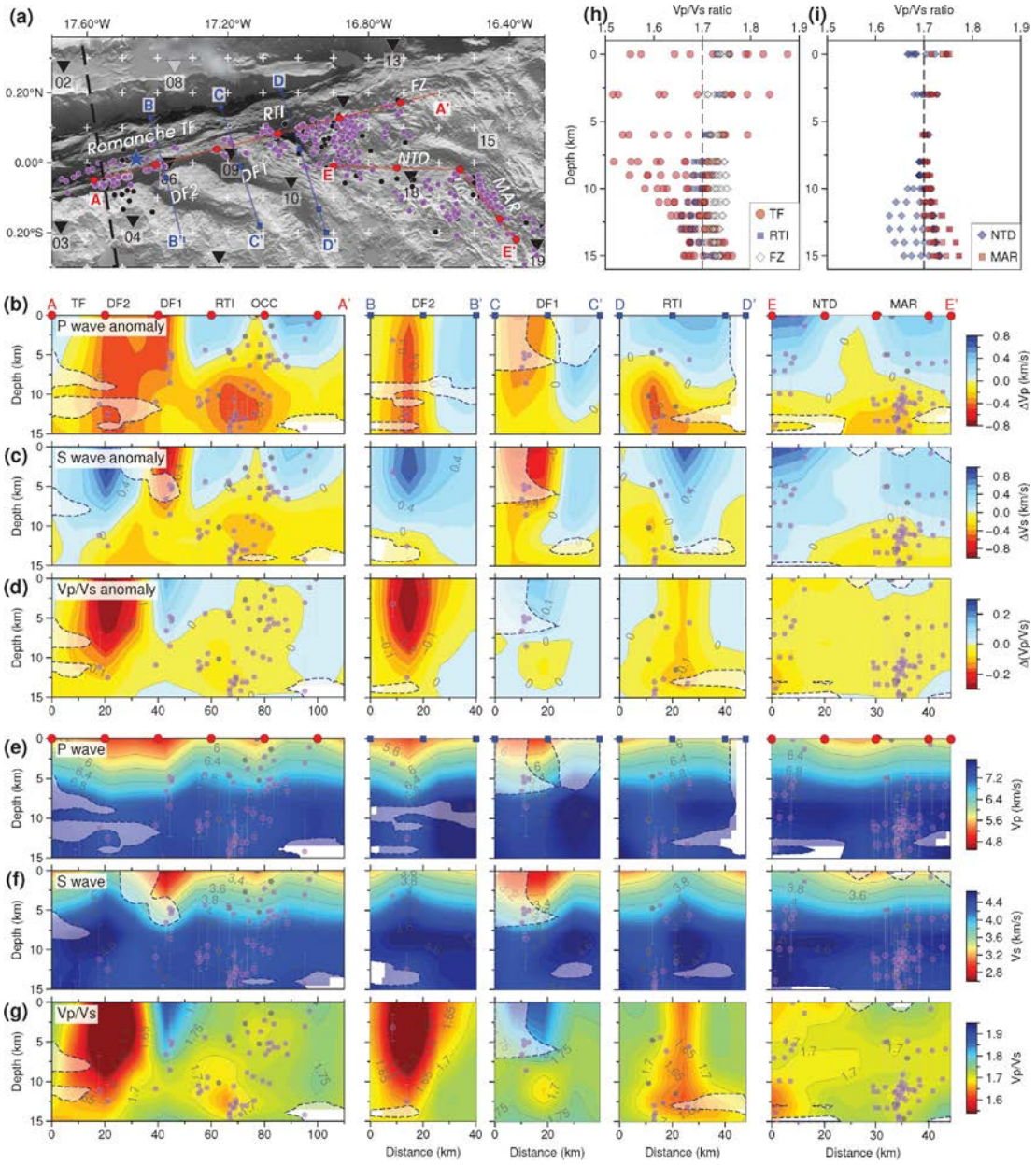

Fig. 7. **Tomographic results** (**a**) Topography and seismicity, showing the location of the cross-sections. The white crosses indicate the grid nodes of the model space. Red and blue lines are five transects shown in (**b**). Five cross-sections of P-wave (**b**) and S-wave (**c**) velocity anomalies, Vp/Vs ratio anomaly (**d**), Vp (**e**), Vs (**f**), and Vp/Vs ratio (**g**) along the Romanche transform (AA′); across the transform fault (BB′, CC′) and RTI (DD′); and along the non-transform discontinuity and the MAR (EE′). The black contour intervals for Vp, Vs and Vp/Vs anomalies are 0.4 km/s (**b**), 0.4 km/s (**c**), and 0.1 (**d**), respectively. The colour scales are shown on the right. Red circles and blue squares on the top indicate the 20-km intervals for reference. The white shade on each map indicates the region that cannot be well restored by the resolution tests in Figs. 5-

6. (**h**) Vp/Vs ratios versus depths along the transform fault, RTI, and fracture zone derived from the profile AA′ (see legend for symbols). (**i**) Vp/Vs ratios along the non-transform discontinuity and MAR derived from the profile EE′. OCC=Oceanic core complex; DF=Detachment fault. The other labelling is the same as that shown in Fig. 1.

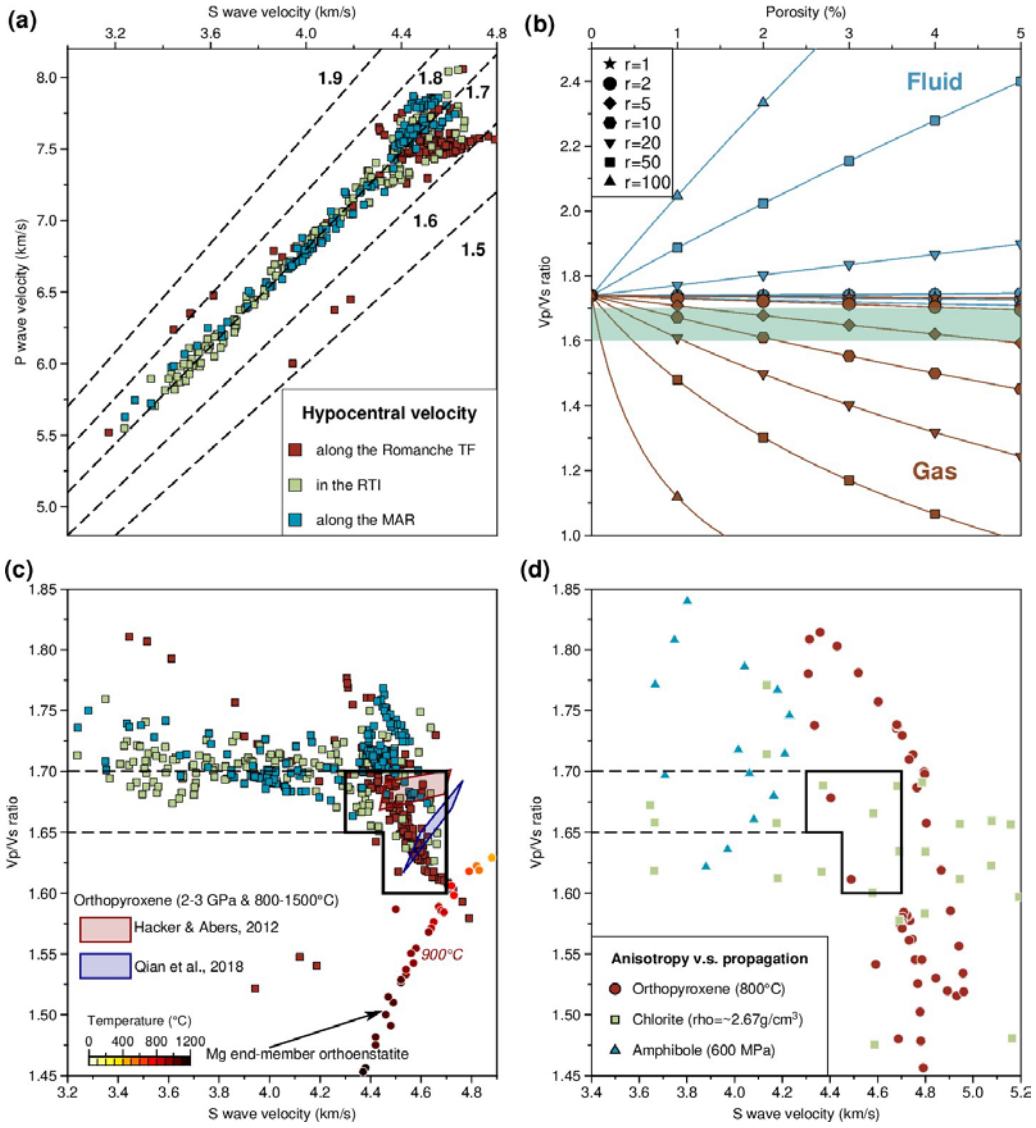

Fig. 8. Vp/Vs ratios. (**a**) P-wave velocity versus S-wave velocity at hypocenters of the used microearthquakes derived from the tomographic results. The dataset is divided into three subsets: earthquakes along the transform fault (red), in the RTI and the fracture zone (green), and along the MAR (blue). (**b**) Vp/Vs ratios as a function of pores filled with gas (red lines) or fluid (blue lines) for various aspect ratios (symbols). The green belt indicates the Vp/Vs ratios between 1.6 and 1.7. (**c**) S-wave velocity and Vp/Vs ratios, compared to the orthopyroxene isotropic velocities. The black (dashed) rectangle represents the unusual values observed in this study. Red and blue rhombuses are the velocities for orthoenstatite at 2-3 Gpa and 800-1500°C (Hacker and Abers, 2012; Qian et al., 2018). The red circles with colour scales are the results for the Mg end-member orthoenstatite as a function of temperature (Jackson et al., 2007). (**d**)

Velocity anisotropy versus wave propagations in the orthopyroxene (red circles) (Jackson et al., 2007), chlorite (green squares) (Mookherjee and Mainprice, 2014), and amphibole (blue triangles) (Ji et al., 2013).

Supporting Information for

Evidence for low Vp/Vs ratios along the eastern Romanche ridge-transform intersection in the equatorial Atlantic Ocean

Zhiteng Yu[1,2*], Satish C. Singh[3], Marcia Maia[1]

[1]*Key Laboratory of Submarine Geosciences, Ministry of Natural Resources, Second Institute of Oceanography, Ministry of Natural Resources, 310012 Hangzhou, China*
[2]*Geo-Ocean UMR6538, CNRS-Ifremer-UBO-UBS, 29280 Plouzané, France*
[3]*Université Paris Cité, Institut de Physique du Globe de Paris, CNRS, Paris, France*

Corresponding authors: Zhiteng Yu (ztyu@sio.org.cn)

Contents of this file

Figures S1 to S13 and a list of references given to citations made in this document.

Additional Supporting Information (Files uploaded separately)

Figure S1. The starting one-dimensional (1-D) velocity models
Figure S2. Density distribution of P-wave rays at different depths.
Figure S3. Density distribution of S-wave rays at different depths.
Figure S4. The first set of resolution tests.
Figure S5. The first set of resolution tests.
Figure S6. The second set of resolution tests.
Figure S7. The second set of resolution tests.
Figure S8. Map views of the inverted P-wave velocities.
Figure S9. Map views of the inverted S-wave velocities.
Figure S10. Map views of the Vp/Vs ratios.
Figure S11. S-P travel times (normalized to the P wave travel time) at different OBS stations.
Figure S12. Histograms of Vp/Vs ratios at the hypocenters of the located microearthquakes.
Figure S13. P-wave velocity versus S-wave velocity as a function of porosity for various aspect ratios using the differential effective medium theory.

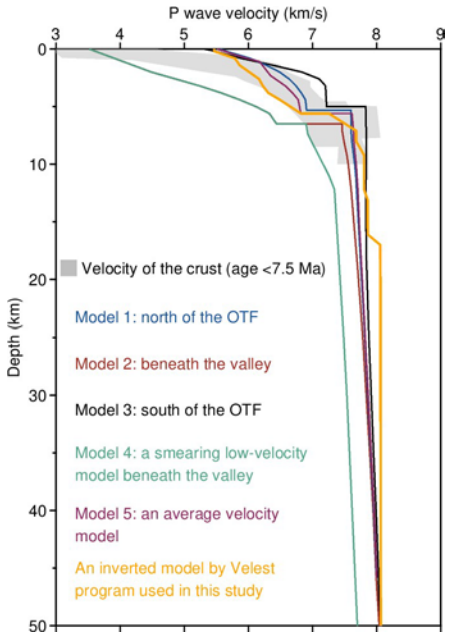

Figure S1. The starting one-dimensional (1-D) velocity models. Five 1-D models (Models 1-5) are derived from an active-source wide-angle seismic refraction profile (Wang et al., 2022). The grey shade represents the velocity of the crust with age less than 7.5 Ma (Christeson et al., 2019). Model 5 is an average velocity model that has been used to locate earthquakes (Yu et al., 2022). The yellow line indicates the "minimum 1-D velocity model" using the VELEST program (Kissling et al., 1994).

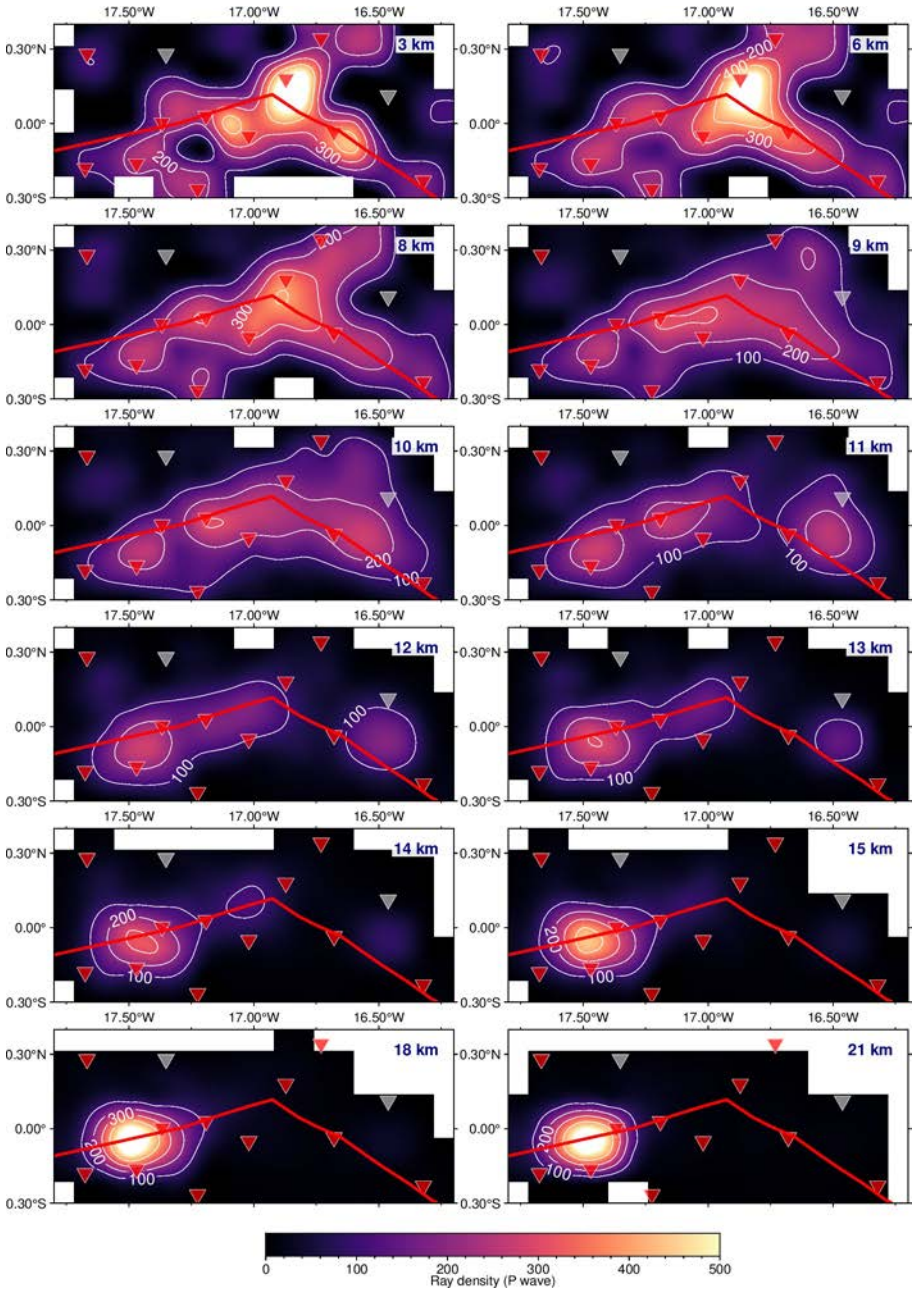

Figure S2. Density distribution of P-wave rays at different depths. The layer depth is shown in the top right corner of each map. The colour scale is shown at the bottom. The red lines show the Romanche transform fault and Mid-Atlantic Ridge (MAR). The red triangles are the deployed ocean-bottom seismometers (OBSs), of which the grey ones were lost or had no data. The contours represent the ray density for P-wave rays.

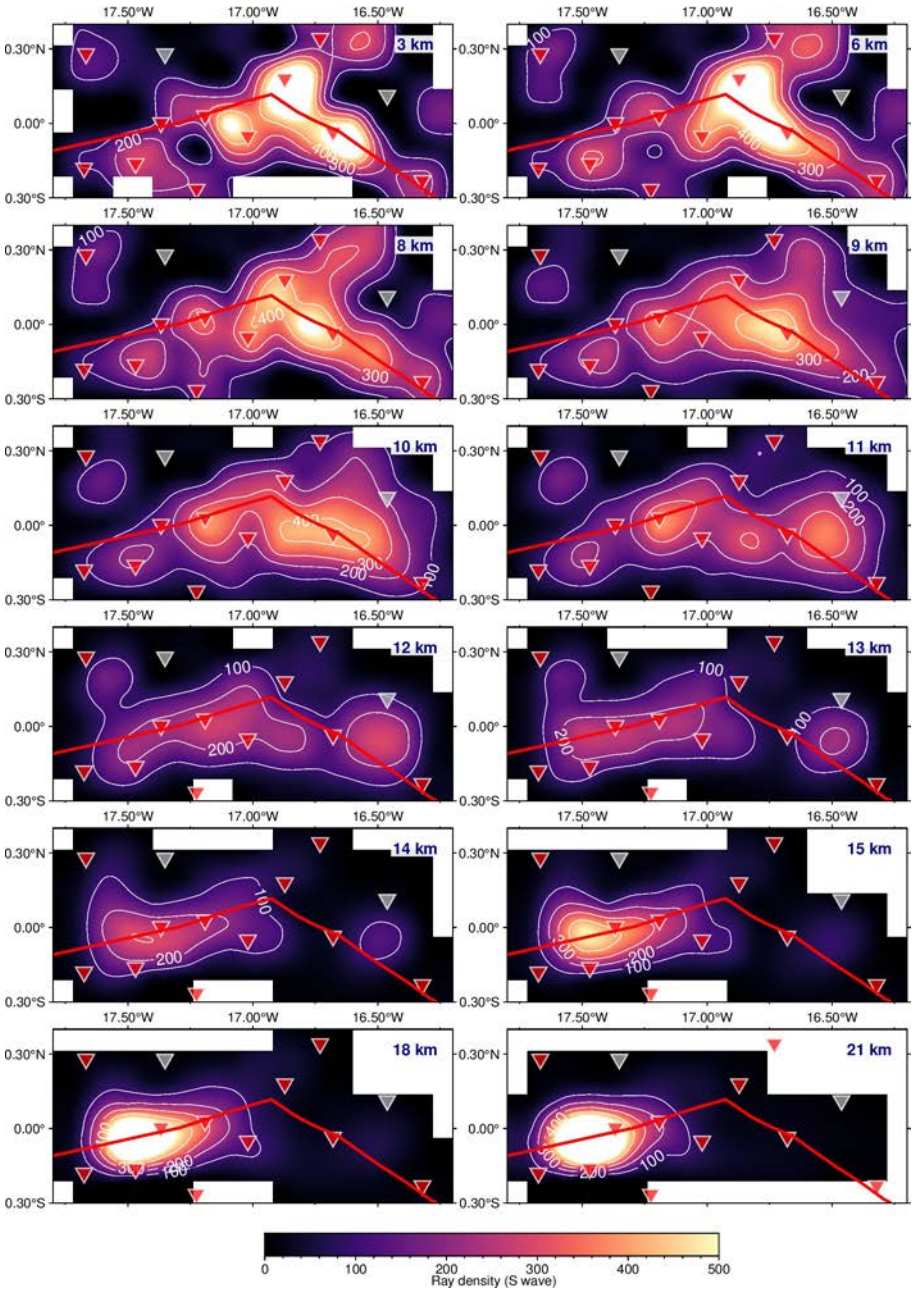

Figure S3. Density distribution of S-wave rays at different depths. The other labelling is the same as that shown in Fig. S2.

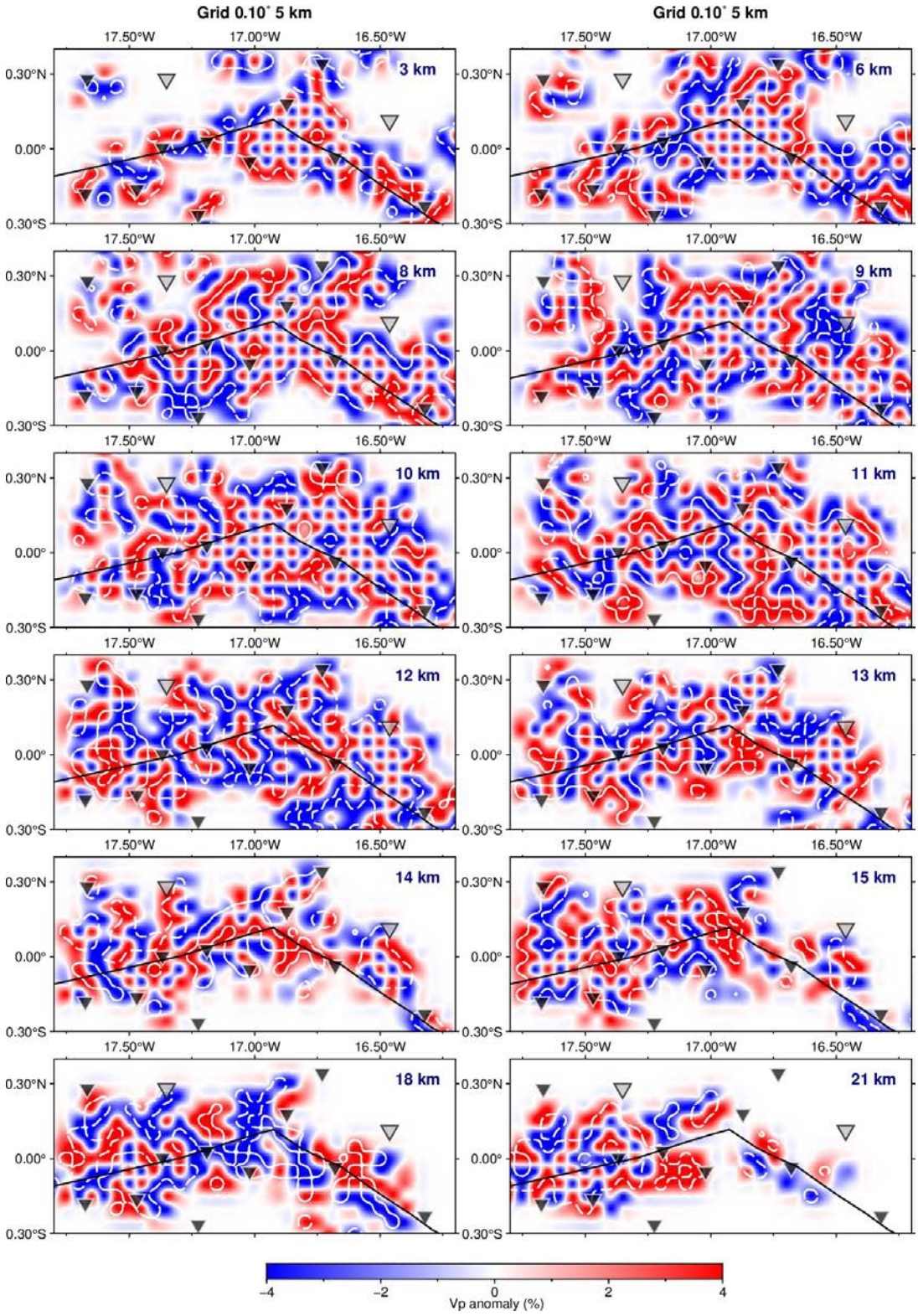

Figure S4. The first set of resolution tests. Results of a checkerboard resolution test for P-wave tomography. The grid interval is 0.05°, ~5 km. The input amplitudes of the velocity perturbations are ±4%, whose scale is shown at the bottom. The thick white dashed lines indicate that the restored amplitudes are greater than 60%. The black triangles are the deployed OBSs, of which the grey ones were lost or had no data. The thick black lines show the Romanche transform fault and MAR. The other labelling is the same as that shown in Fig. S2.

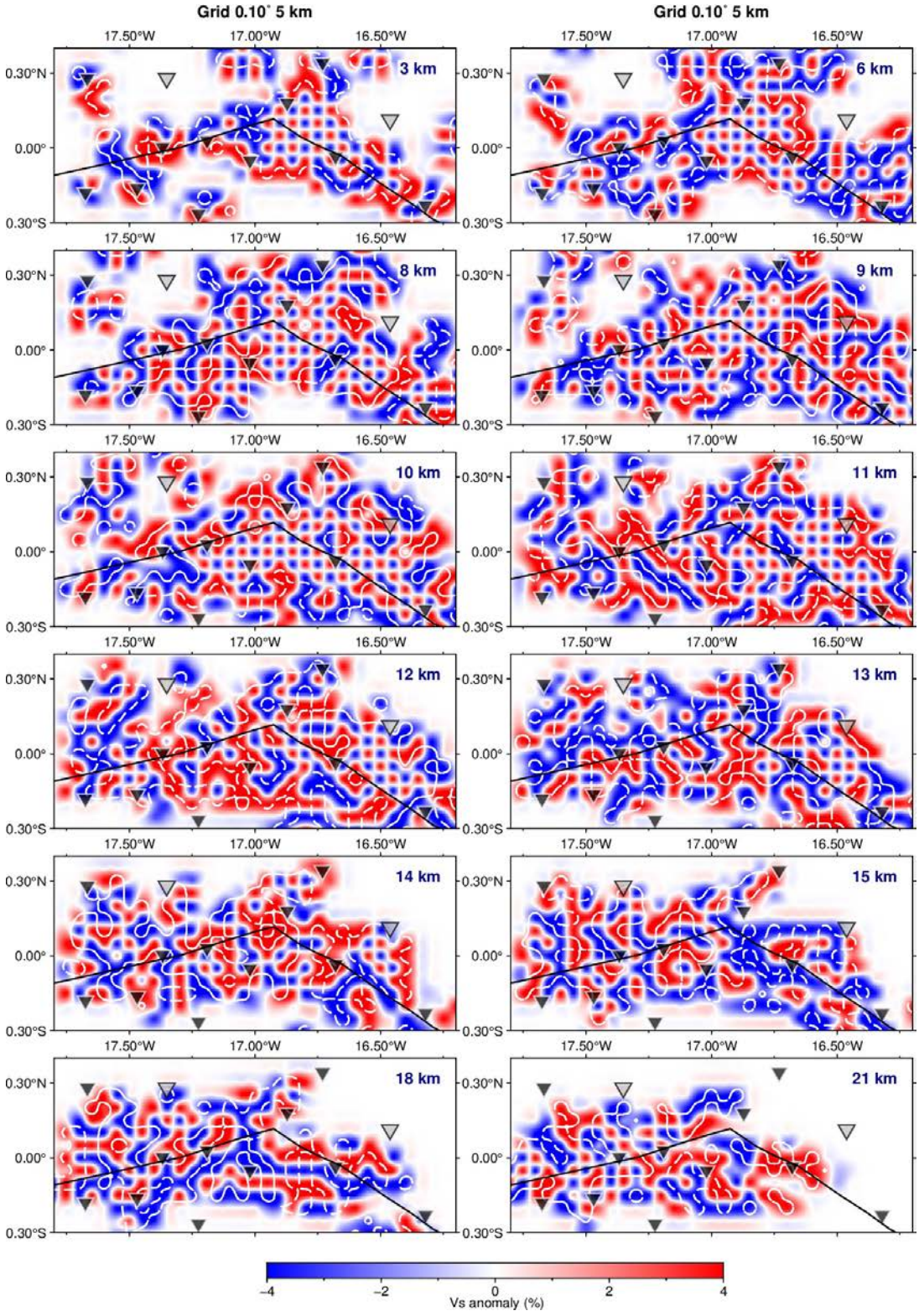

Figure S5. The first set of resolution tests. The same as Fig. S4 but for S-wave tomography.

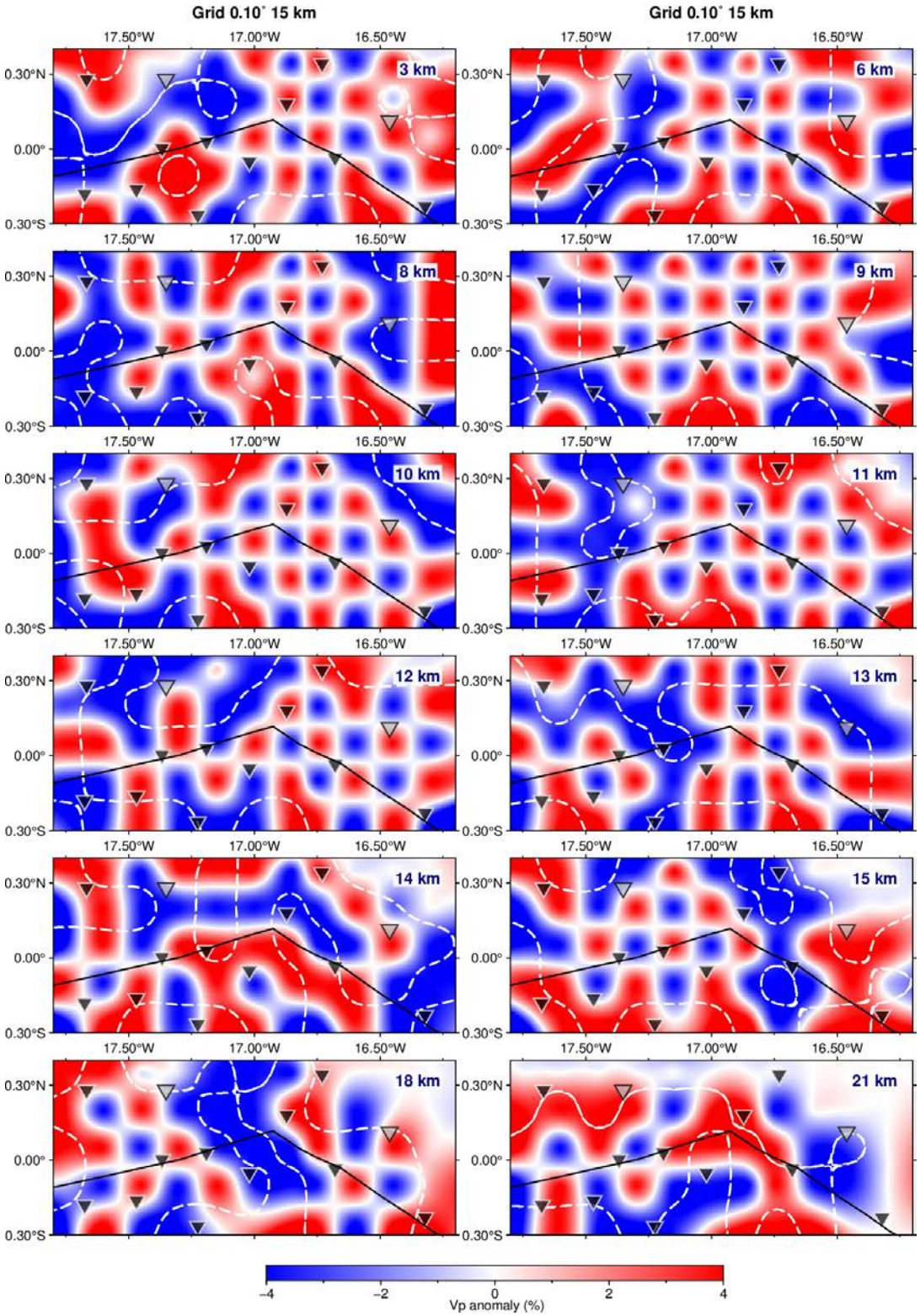

Figure S6. The second set of resolution tests. The same as Fig. S4 but the grid interval is 0.15°, ~15 km.

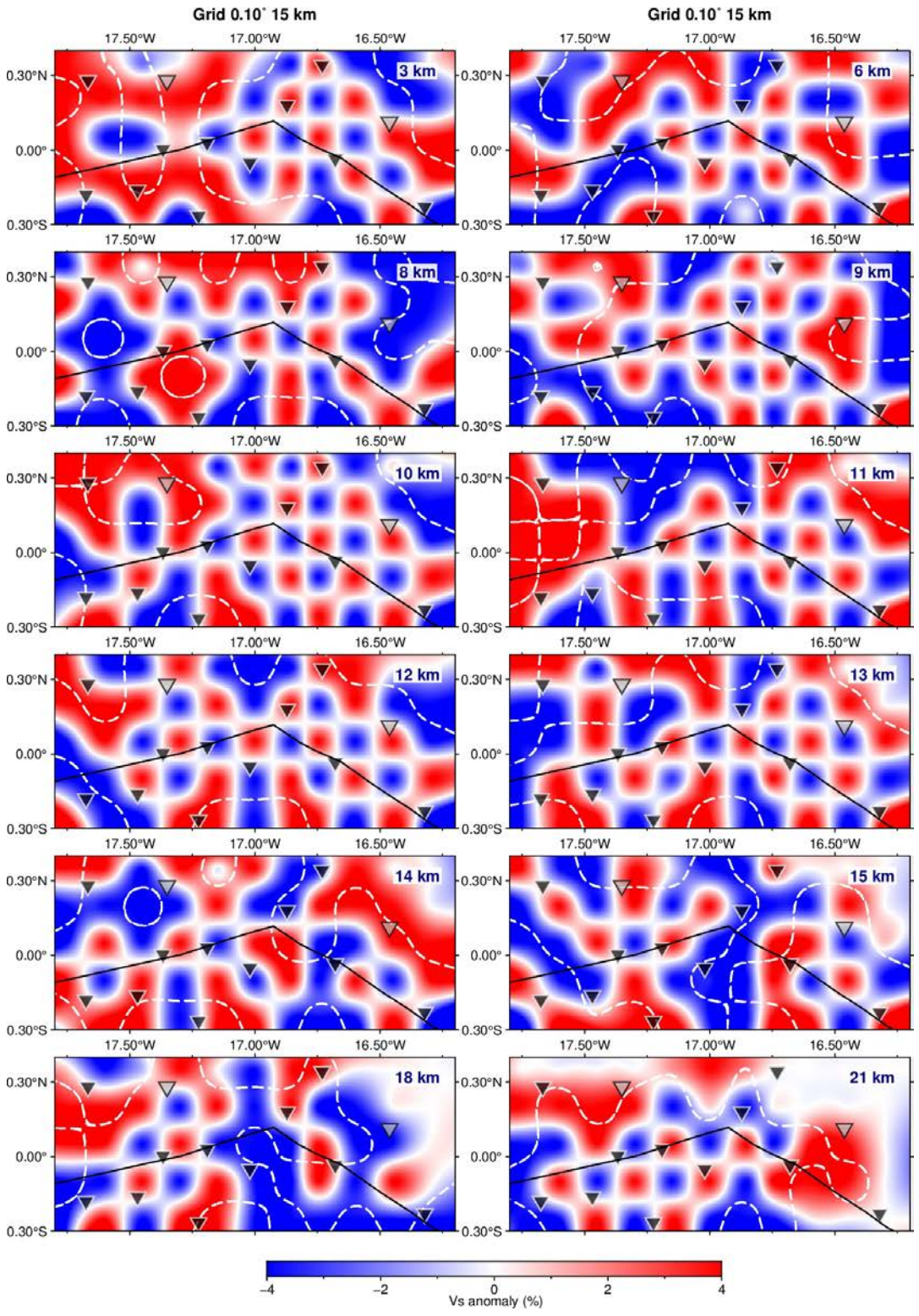

Figure S7. The second set of resolution tests. The same as Fig. S6 but for S-wave tomography.

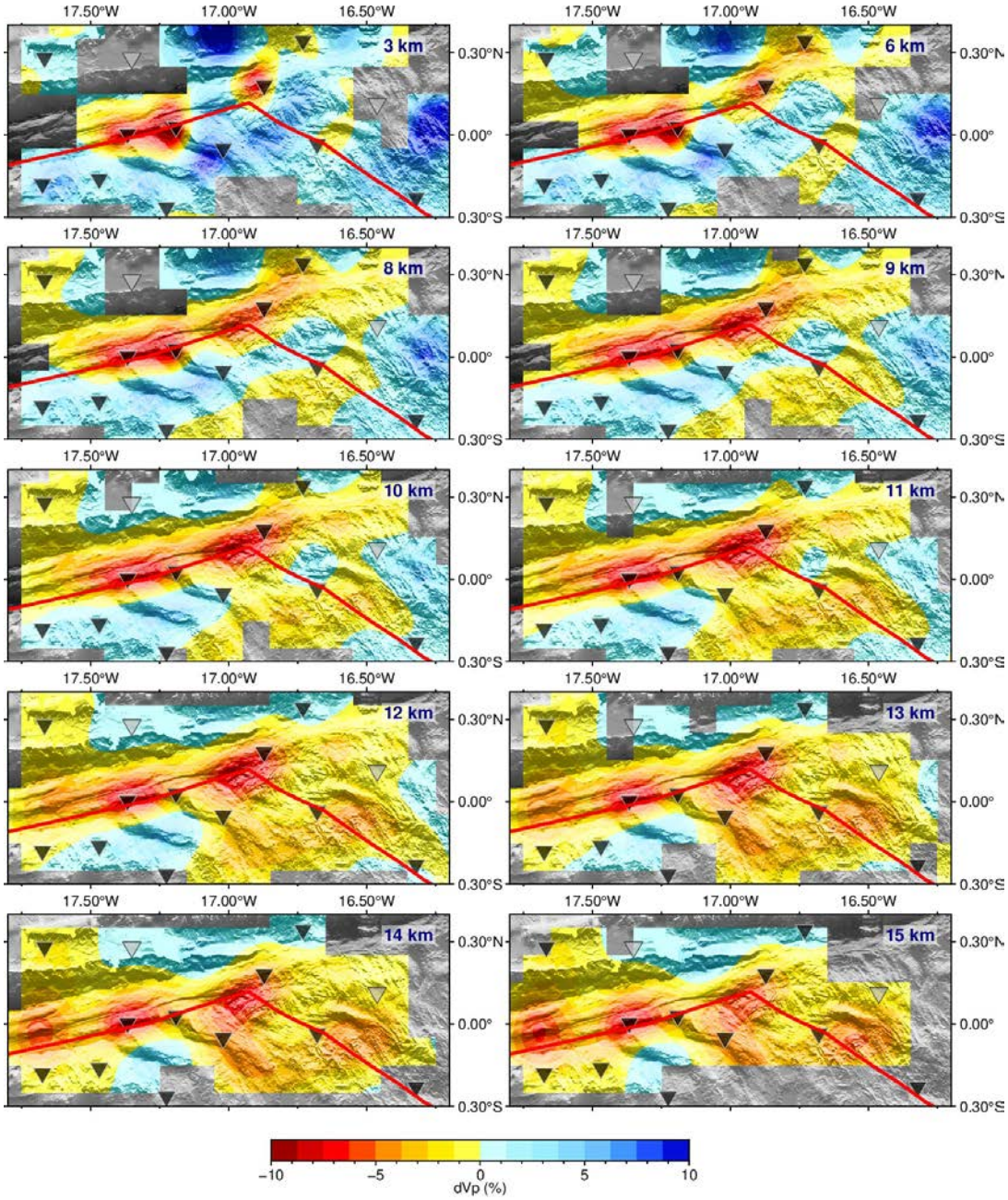

Figure S8. Map views of the inverted P-wave velocities. The lateral grid spacing is 0.10°. The red colour indicates low-velocity anomalies, whereas the blue colour indicates high-velocity anomalies, whose scales are shown at the bottom. The black triangles are the deployed OBSs, of which the grey ones were lost or had no data. The other labelling is the same as that shown in Fig. S2.

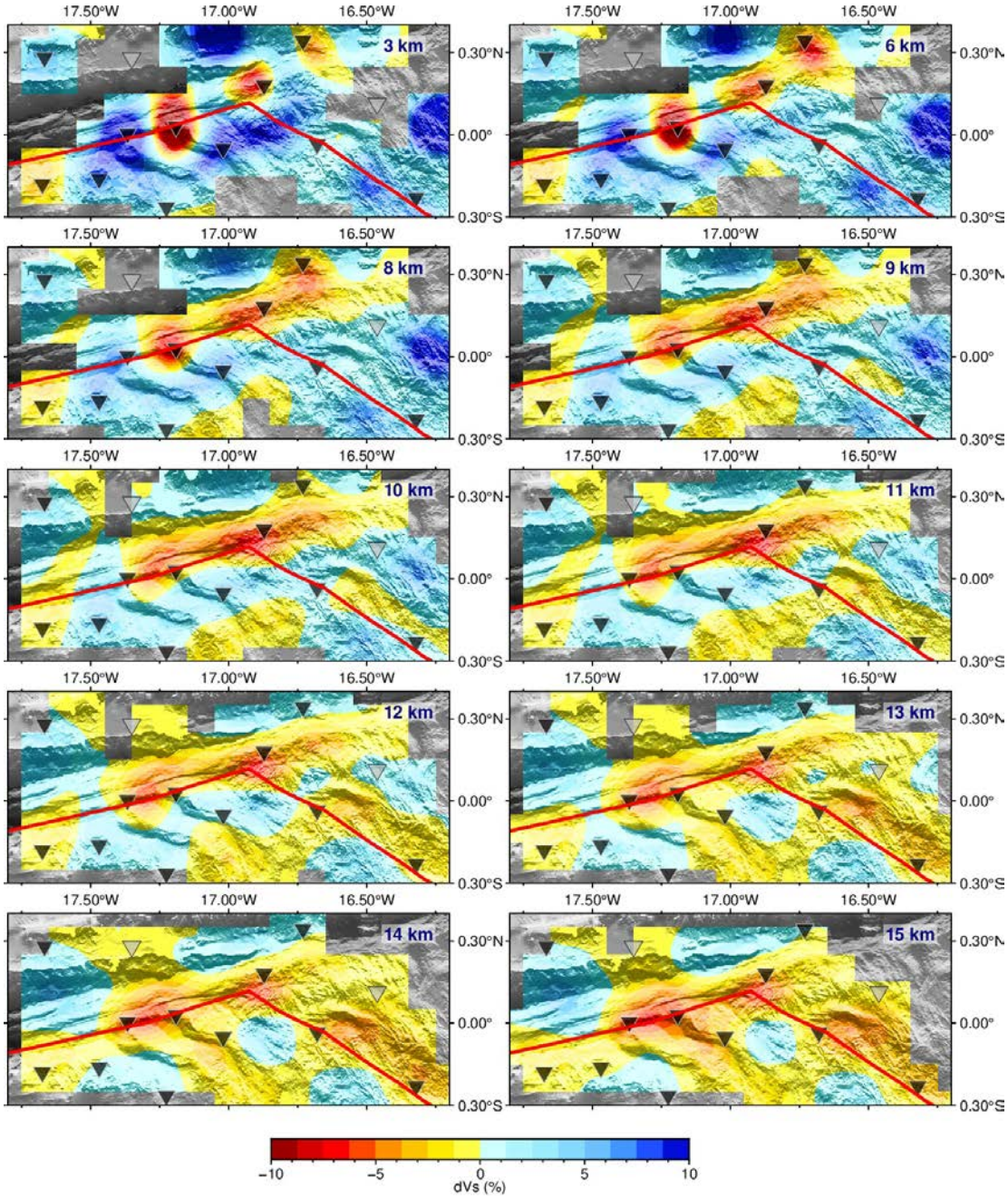

Figure S9. Map views of the inverted S-wave velocities. The other labelling is the same as that shown in Fig. S8.

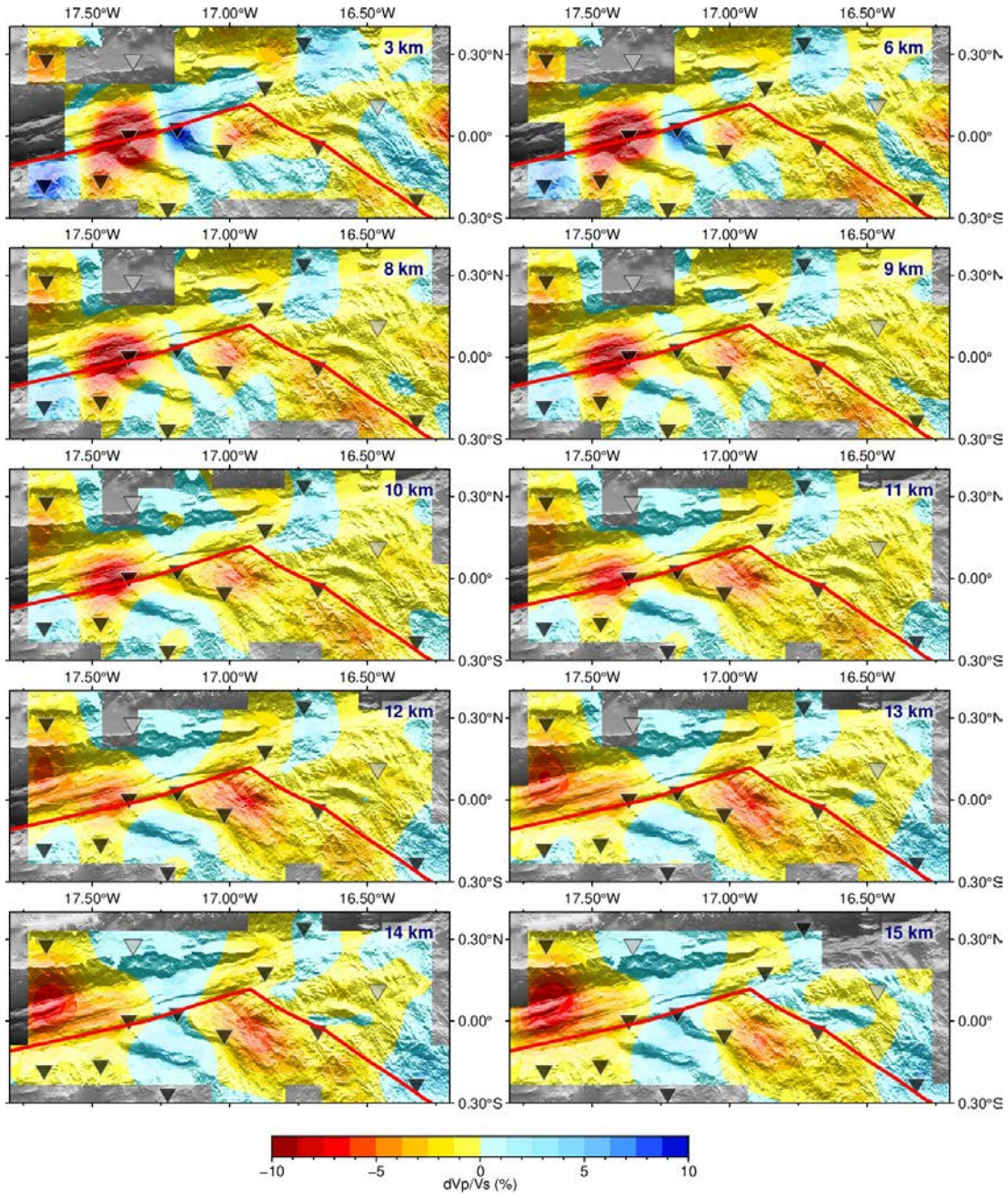

Figure S10. Map views of the Vp/Vs ratios. Red and blue colours indicate Vp/Vs ratio anomalies in reference to the ratio of 1.73, respectively. The other labelling is the same as that shown in Fig. S8.

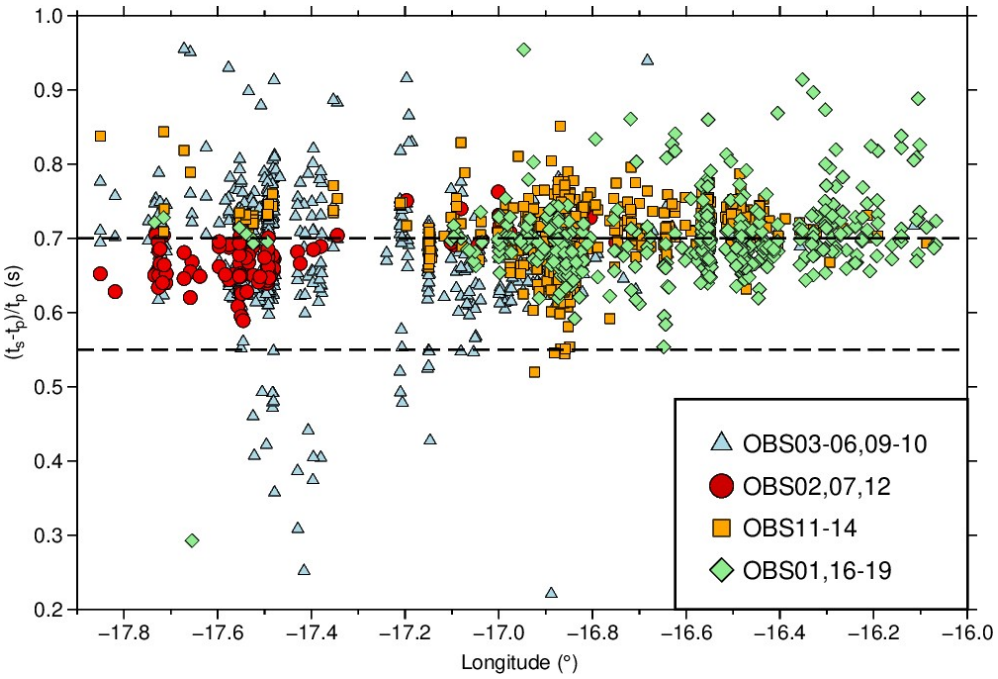

Figure S11. S-P travel times (normalized to the P wave travel time) at different OBS stations. The blue triangles show the S-P times ($(t_s-t_p)/t_p$) along the southern Romanche transform fault at OBSs 03-06, 09-10; the red circles show the results in the north of the Romanche transform fault (OBSs 02,07, and 12); the brown squares indicate the results in the RTI region (OBSs 11-14); the green diamond marks these values along the Mid-Atlantic Ridge (OBSs 01, and 16-19). The location of OBS stations could be found in Figs. 1 and 7.

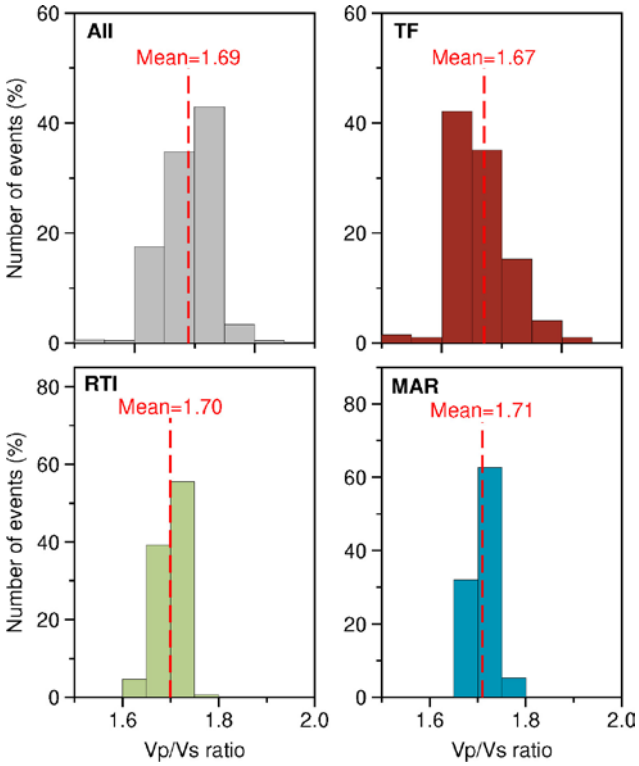

Figure S12. Histograms of Vp/Vs ratios at the hypocenters of the located microearthquakes. Red, green, and blue columns show the ratios for earthquakes located along the transform fault (TF), in the ridge-transform intersection (RTI), and along the MAR, respectively.

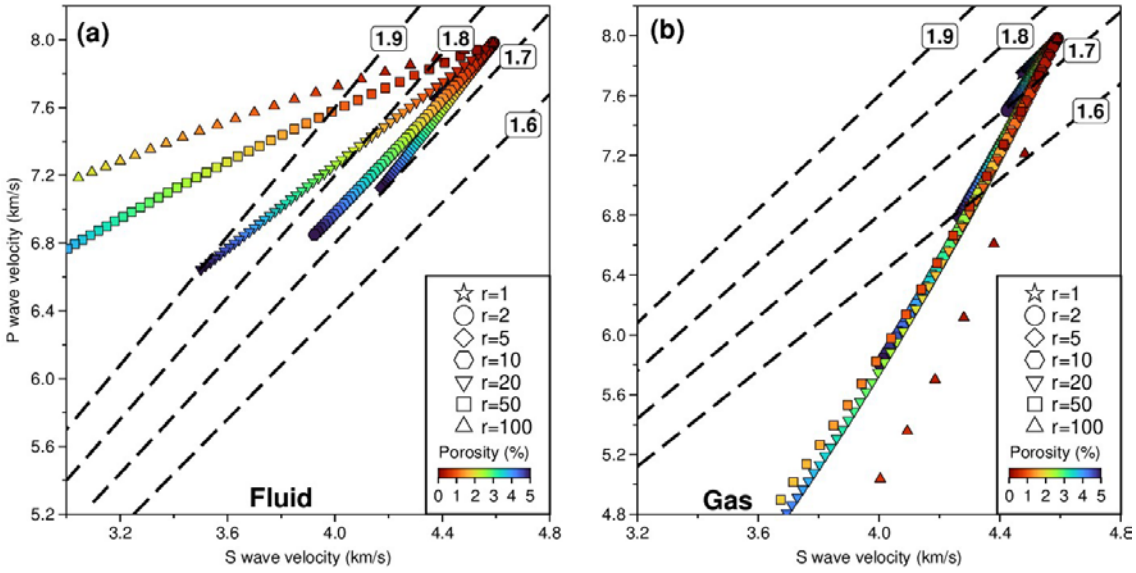

Fig. S13. P-wave velocity versus S-wave velocity as a function of porosity for various aspect ratios using the differential effective medium theory (Taylor and Singh, 2002). (**a**) Pores filled with fluid (water). The different symbols (star, circles, diamond, hexagon, inverted triangle, square, and triangle) indicate various aspect ratios ranging from 1 (spherical inclusion) to 100 (thin film). The porosity varies from 0% to 5%, whose colour scale is shown in the inset map. Four dashed lines indicate the Vp/Vs ratios from 1.6 to 1.9. (**b**) Pores filled with gas. The other labelling is the same as that shown in (**a**).

References

Christeson, G.L., Goff, J.A., and Reece, R.S., 2019, Synthesis of Oceanic Crustal Structure From Two-Dimensional Seismic Profiles: Reviews of Geophysics, v. 57, p. 504–529, doi:10/gnq6h9.

Kissling, E., Ellsworth, W.L., Eberhart-Phillips, D., and Kradolfer, U., 1994, Initial reference models in local earthquake tomography: Journal of Geophysical Research: Solid Earth, v. 99, p. 19635–19646, doi:10.1029/93JB03138.

Taylor, M.A.J., and Singh, S.C., 2002, Composition and microstructure of magma bodies from effective medium theory: Geophysical Journal International, v. 149, p. 15–21, doi:10.1046/j.1365-246x.2002.01577.x.

Wang, Z., Singh, S.C., Prigent, C., Gregory, E.P.M., and Marjanović, M., 2022, Deep hydration and lithospheric thinning at oceanic transform plate boundaries: Nature Geoscience, v. 15, p. 741–746, doi:10.1038/s41561-022-01003-3.

Yu, Z., Singh, S., Grenet, L., Maia, M., Hamelin, C., Briais, A., Petracchini, L., and Brunelli, D., 2022, CO2 degassing in the mantle triggers deep earthquakes at the Mid-Atlantic Ridge: In Review preprint, doi:10.21203/rs.3.rs-1945608/v1.